CHAPTER III

RESULTS AND DISCUSSION

3.1 Gravitational Field-Flow Fractionation Instrumentation

3.1.1 Cost-effective Gravitational FFF System

This section describes the gravitational FFF instrumentation and ancillary equipment used [74].

FFF instrumentation can be similar to high performance liquid chromatography (HPLC), although in some cases, FFF systems may be more complicated. There are now FFF instruments commercially available [38, 39], but they are rather expensive, especially in comparison to research budgets available in Thailand. Therefore we are interested in making use of existing components, not only for basic research but also in term of instrumental development. The following presents the possibilities for cost-effective set-ups for gravitational FFF (GrFFF).

A GrFFF system usually consists of the five components represented schematically in Figure 3.1 [75-77].

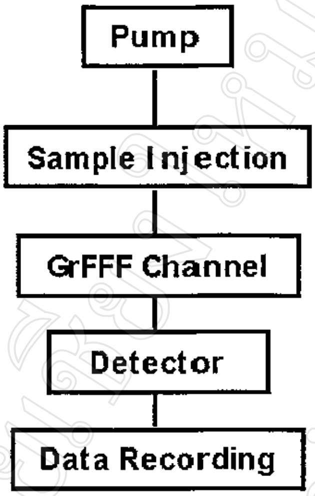

Figure 3.1 Schematic diagram of a simple GrFFF system

Many alternatives for components of a GrFFF system exist and some of those are listed below.

3.1.1.1 Pumping System

A pumping system is required to deliver the carrier flow to the channel. It may be one of the following:

1. A gas pressure device; this usually utilizes a cylinder of an inert gas (e.g. N_2) to propel the carrier solution [16,59].
2. A peristaltic pump; uses a flexible tubing placed within the rotation head and the flow rate can be adjusted via rotation speed of the pump head. This is usually used for flow injection analysis.
3. An HPLC pump; commonly a reciprocating piston pump; often with dual pistons for continuous operation reducing pulsing [78].

4. A syringe pump; a larger volume displacement pump, may be employed which give no pulsing [78].

HPLC pumps are rather expensive, though they are efficient options. Peristaltic pumps are less expensive but suffer from pressure and flow pulsing. They are widely used in FIA and FFF work. N_2 gas pressured propulsion is a cheap option, which should be available in general laboratories having a compressed N_2 gas cylinder or line. One advantage of the gas pressure pump is that it produces pulse free output. However, accurate control of the pressurized gas can be difficult and required a good quality regulator.

In this work, a peristaltic pump was used at the initial stages as it was available in our FIA laboratory at Chiang Mai. An HPLC pump was also employed in some experiments. N_2 gas pressurized system has been employed in our undergraduate laboratory projects.

3.1.1.2 Injection System

Sample injection for the GrFFF can be achieved using one of the methods below:

1. Home made injection device: this was made from a plastic block (Figure 3.2). A sample is injected into carrier stream via a silicone rubber septum with a hypodermic syringe needle.
2. 6-port injection valve: this type of valve is commercially available from various suppliers, for example, Rheodyne, Hamilton or Upchurch.

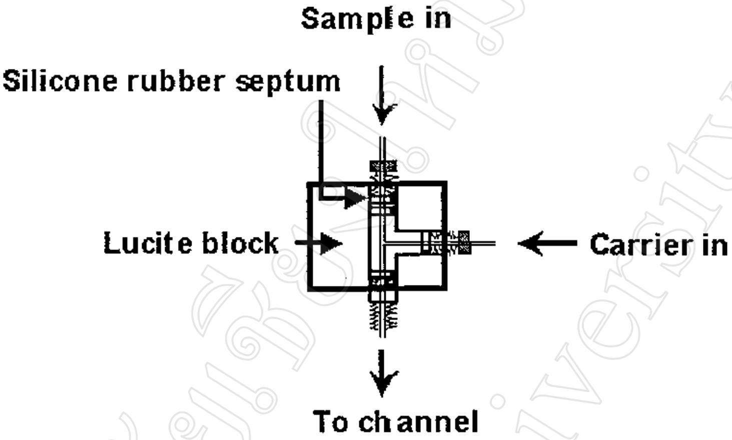

Figure 3.2 A home made injection port

3.1.1.3 Separation System (GrFFF Channel)

FFF separation unit, The FFF channel is a thin open i.e. unpacked rectangular ribbon with triangular inlet and outlet end pieces. Typical dimensions are 20–100 cm x 1–2 cm x 0.01–0.05 cm. The construction of a GrFFF channel is described in Section 2.4.1.

3.1.1.4 Detection System

The detectors that have been employed include the following: a UV/Vis detector [79], fluorescence detector or a light scattering (LS) detector [80,81], laser-induced breakdown detection (LIBD) [82,83], multi-angle laser light scattering (MALLS) [84-86], thermal lens detection [87] and chemiluminescence detection [88].

3.1.1.5 Recording System

The acquisition/read-out unit could be a chart recorder, low-cost interfacing device (simple computer-interfacing device such as Pocket Sampler, which is commercially available (Dick Smith, Australia)) or a more comprehensive computer package such as LabVIEW (National Instruments™, USA).

3.1.2 GrFFF Fractograms and Retention Order

3.1.2.1 GrFFF Fractograms

The GrFFF fractogram is obtained by using a chart recorder or digitized signal from the interface and is a plot of the detector response versus elution time. However, it is often advantageous to convert the x-axis to elution volume as this compensates for changes in flow rate in different GrFFF runs.

3.1.2.2 GrFFF Retention Order

The first peak eluted is a void peak due to dissolved material or unretained particles which may be either too small to be settled by the gravitational field or so large that retention is negligible. The subsequent retained peaks are due to the sample particles. The mean retention can be characterized by the position of the peak maximum signified by t_r and V_r for time and volume measurements respectively. GrFFF operates in the steric/hyperlayer mode of FFF thus larger particles elute before smaller ones.

3.1.3 Performance Testing of GrFFF with Silica Gel 60G (<40 μm)

The GrFFF was tested using two size fractions of silica gel. This demonstrated the trends in retention under various run conditions. This series of experiments could be an ideal student laboratory exercise for illustrating many of the important principles of separation science.

A simple GrFFF consisting of a peristaltic pump, six-port injection valve, a GrFFF channel, a UV/Vis detector and chart recorder was tested using a sample of thin layer chromatography silica gel 60. The silica gel had a reported size range of 5-40 μm, however, it was found that it contains some fine particles (<5 μm). The broad silica size ranges of <10 μm and 10-20 μm were prepared from original silica gel (<40 μm) by repeated settling method (as outlined in Section 2.3.1) [89].

3.1.3.1 Effect of Flow Rate

The results presented in Figure 3.3 show that the lower the flow rate, the higher the retention volume. The retention volumes of sample peaks (the second peak in the fractorgram) had a value of 2, 2.8 and 3.4 mL at flow rates of 3.0, 2.0 and 1.5 mL min^{-1}, respectively. This demonstrates that the lift forces are stronger at higher flow rates, which elevates the particles further away from the accumulation wall and will move into the higher velocity flow streams.

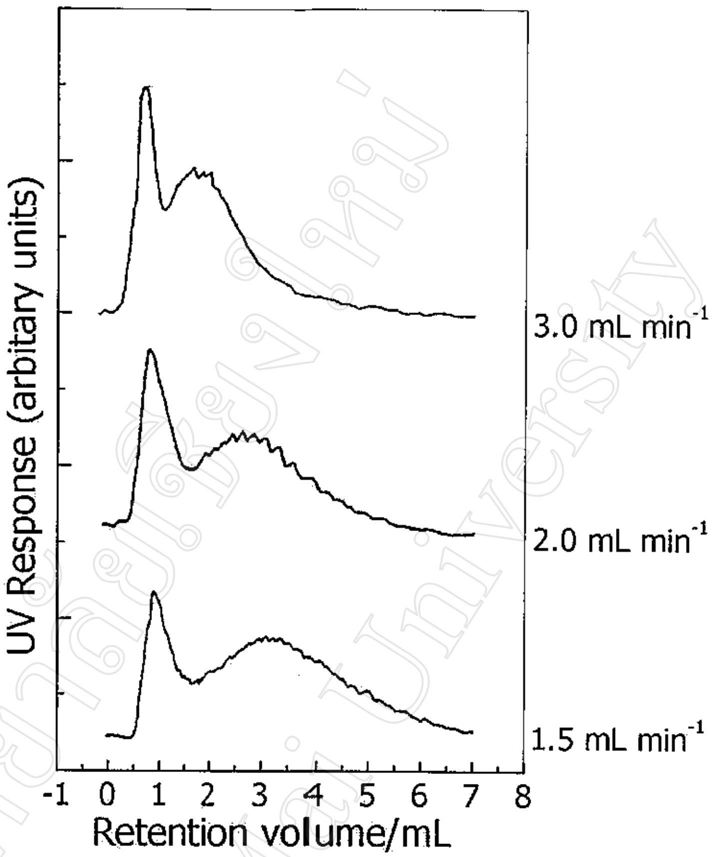

Figure 3.3 The fractograms of silica gel <10 μm with different flow rate. The carrier was H_2O with relaxation time of 30 s

3.1.3.2 Effect of Relaxation Time

Figure 3.4 shows effect of relaxation time on retention of <10 μm silica particles. The relaxation times of 30, 60, 90, 120 and 150 s were investigated. The peaks are shifted under different relaxation time conditions. The retention volume at the peak maximum increased from 3.0 mL to 4.0 mL as t_{relax} from 30 s to 150 s (see Figure 3.4). It can be seen that slightly broader peak was obtained when the relaxation time increased. Since the calculated relaxation time is only 15 s (equation 1.1), the stop flow relaxation procedure could be safely eliminated with this sample since effective settling occurs early in the sample migration.

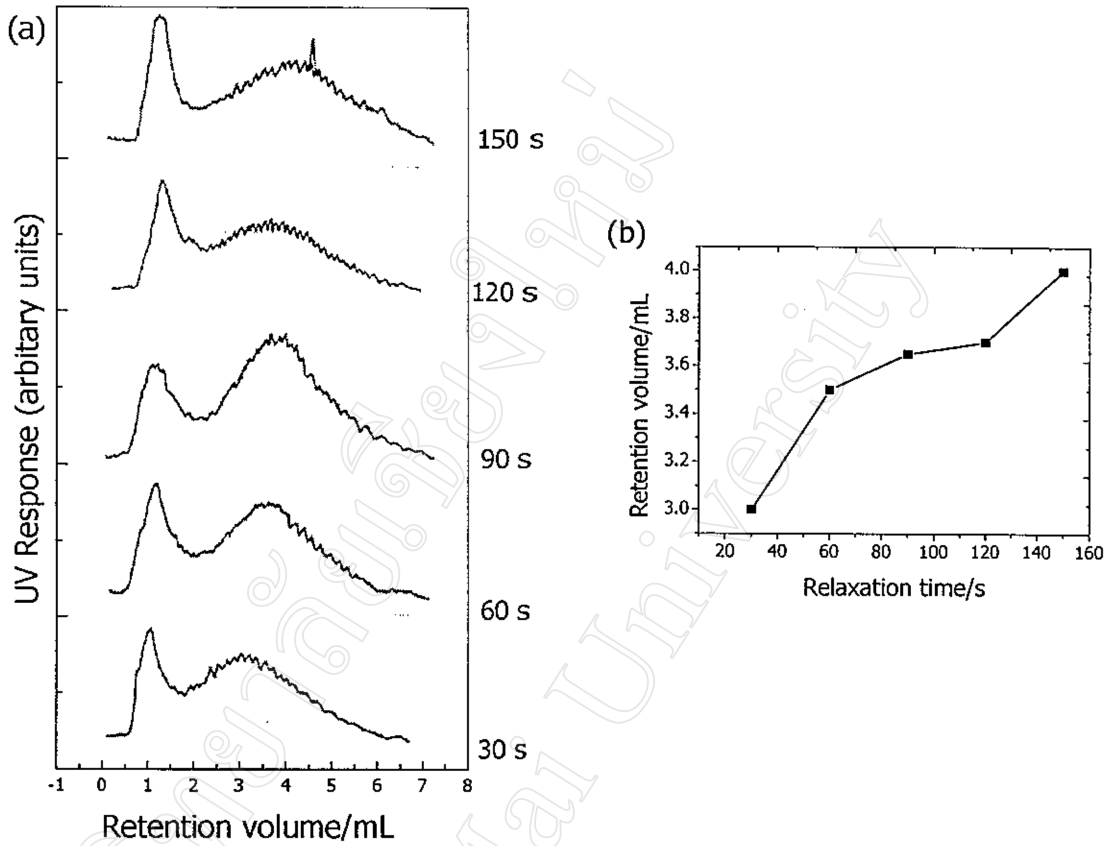

Figure 3.4 (a) The fractograms of silica gel <10 μm with different relaxation time, carrier was H_2O, at flow rate of 1.5 mL min^{-1}. (b) Plot of retention volume (V_r) vs relaxation time (t_{relax})

3.1.3.2 Effect of Particle Size on Retention

Retention of the two different size ranges of particles are shown in Figure 3.5. The fractogram of mixture (1:1) of 10-20 μm and <10 μm shows separation under the run conditions. It was found that the bigger particles the lower retention volume. This is expected for steric/hyperlayer mode runs [10-12].

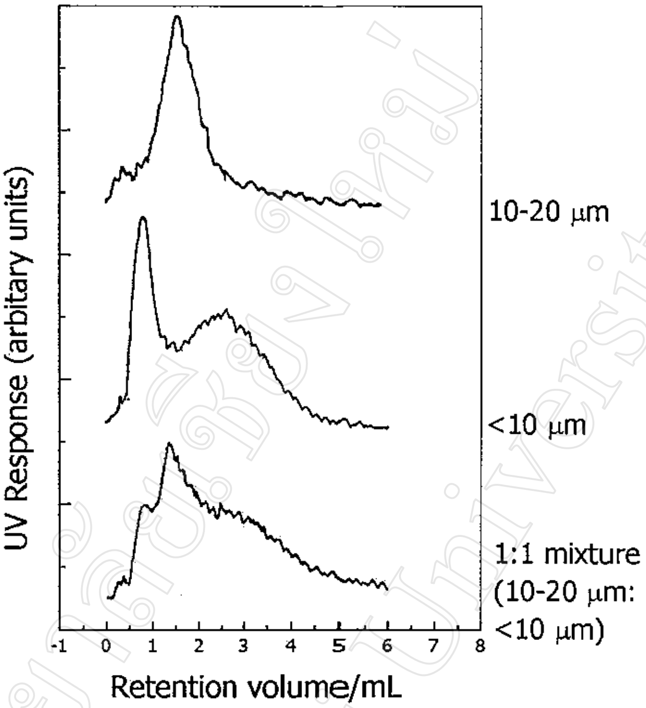

Figure 3.5 Fractograms of silica samples size ranges of 10-20 μm and <10 μm, and a mixture(1:1) of 10-20 μm and <10 μm. The carrier was H_2O, the flow rate 2.0 mL min^{-1}, and relaxation time was 30 s

3.1.4 Separation of Chromatographic Silica (5 μm and 10 μm) by Gravitational Field-Flow Fractionation

In these investigations, the instrument set up as shown in Figure 2.3 was used. The carrier was 10^{-4} M sodium hydroxide and two samples of chromatographic silica (5 μm and 10 μm) were used at a suspension concentration of 2 mg mL^{-1} with an injection volume of 20 μL. The effect of sample loading and channel flow rates are discussed below.

3.1.4.1 Sample Overloading

In FFF separations the amount of sample loading is important. In this study, different volumes (6, 10, 20, 30, 40 and 50 μL) of 5 μm silica particles suspension with a concentration 2 mg mL^{-1} were loaded onto the GrFFF channel. The carrier was 10^{-4} M sodium hydroxide with a flow rate of 1.00 mL min^{-1}. The results obtained are represented in Figure 3.6.

The injected volumes of 6, 10, 20, 30, 40 and 50 μL can be converted to the mass of silica giving 12, 20, 40, 60, 80 and 100 μg, respectively. The results showed that the peak maximum retention time shifted when the sample load was beyond 20 μL or 40 μg of silica. In all further work, the sample load was not more than 20 μL.

Figure 3.7 shows a plot between the mass of silica injected and the area under the sample peak. A linear relationship was obtained which indicates that the sample recoveries for this series of runs are good. If sample losses occur, this is usually dependent on the sample load leading, to curvature and the line may not extrapolate to the origin.

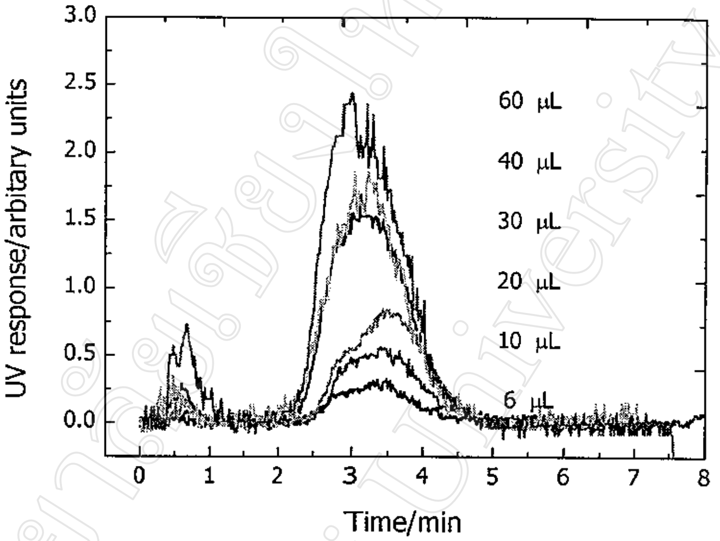

Figure 3.6 Fractograms of the 5 μm chromatographic silica particles at different sample loading

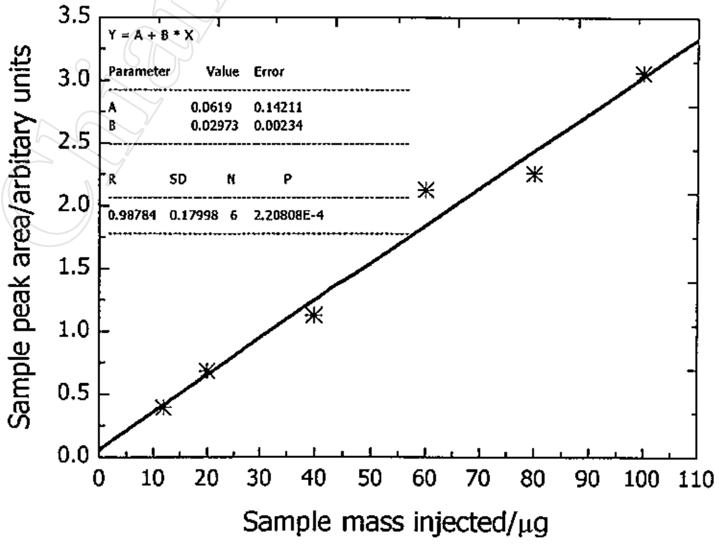

Figure 3.7 Plot of sample mass loading vs sample peak area

3.1.4.2 Effect of Flow Rate

Figures 3.8 and 3.9 depict the fractograms of the 5 μm and 10 μm silica, respectively for at flow rates of 0.20, 0.40, 0.60 and 1.00 mL min^{-1}. The higher flow rate results in observing a lower retention time. More significantly, the elution volume at the peak maximum shifts to a lower retention volume as the flow rate increases (Figure 3.10a). Consequently, the retention ratio increases at higher flow rates (Figure 3.10b). This demonstrates that the lift forces are stronger at higher flow rates which elevates the particles further away from the accumulation wall and experience the higher velocity flow streams.

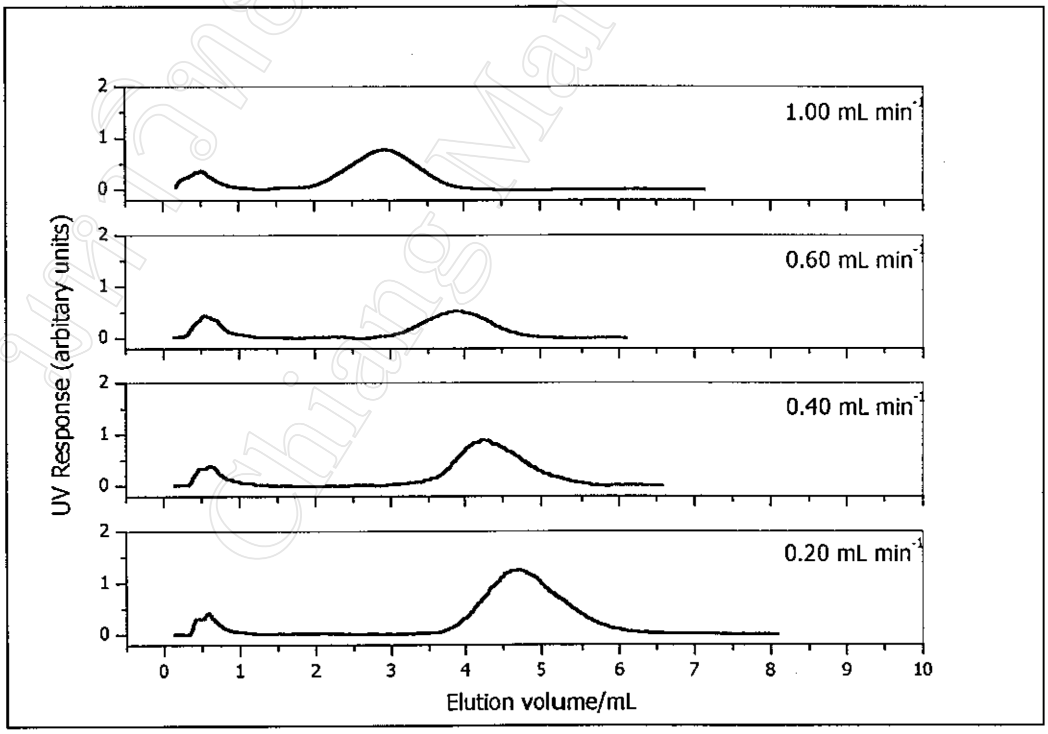

Figure 3.8 Fractograms of the 5 μm chromatographic silica particles at different flow rates

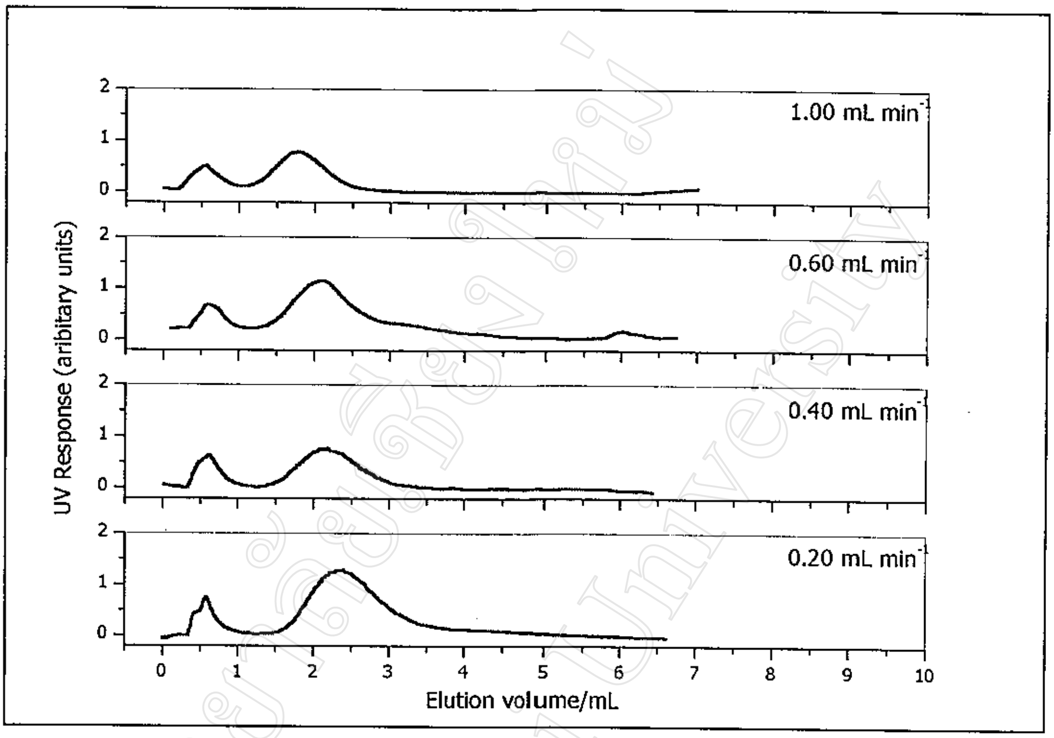

Figure 3.9 Fractograms of the 10 μm chromatographic silica particles at different flow rates

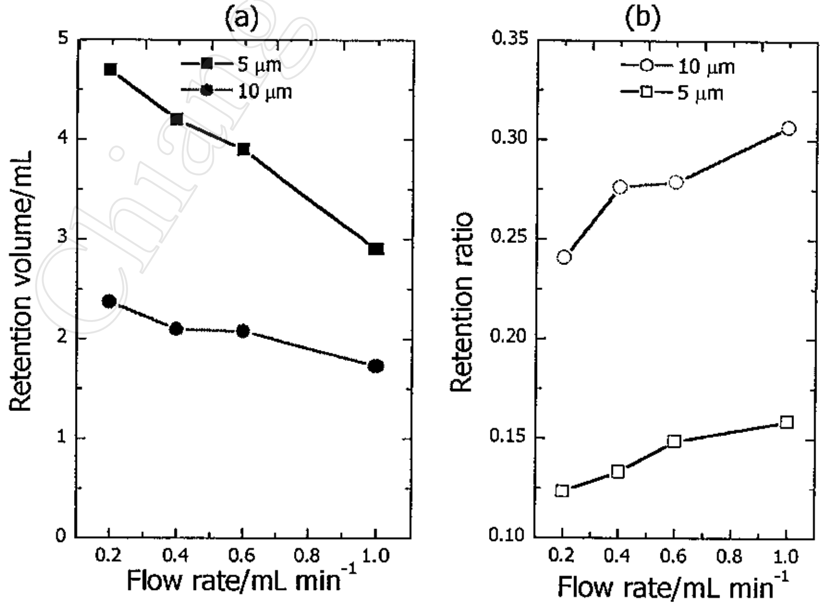

Figure 3.10 Effect of flow rate on (a) retention volume and (b) retention ratio of 5 μm and 10 μm silica particles

3.2 Reverse Flow Injection Analysis with Chemiluminescence Detection by Liquid Scintillation Counter

3.2.1 Liquid Scintillation Counter as a Chemiluminescence Detector

In this section the sensitive determination of iron by a flow injection (FI) system with chemiluminescence detection (CL) is demonstrated. The method is based on the catalytic reaction of alkali luminol (5-amino-2,3-dihydrophthalazine-1,4-dione) and hydrogen peroxide. Trace amounts of iron catalyze the luminol oxidation, which emits light [60-66, 68-71]. Figure 3.11 shows the reactions of the luminol which produce chemiluminescence.

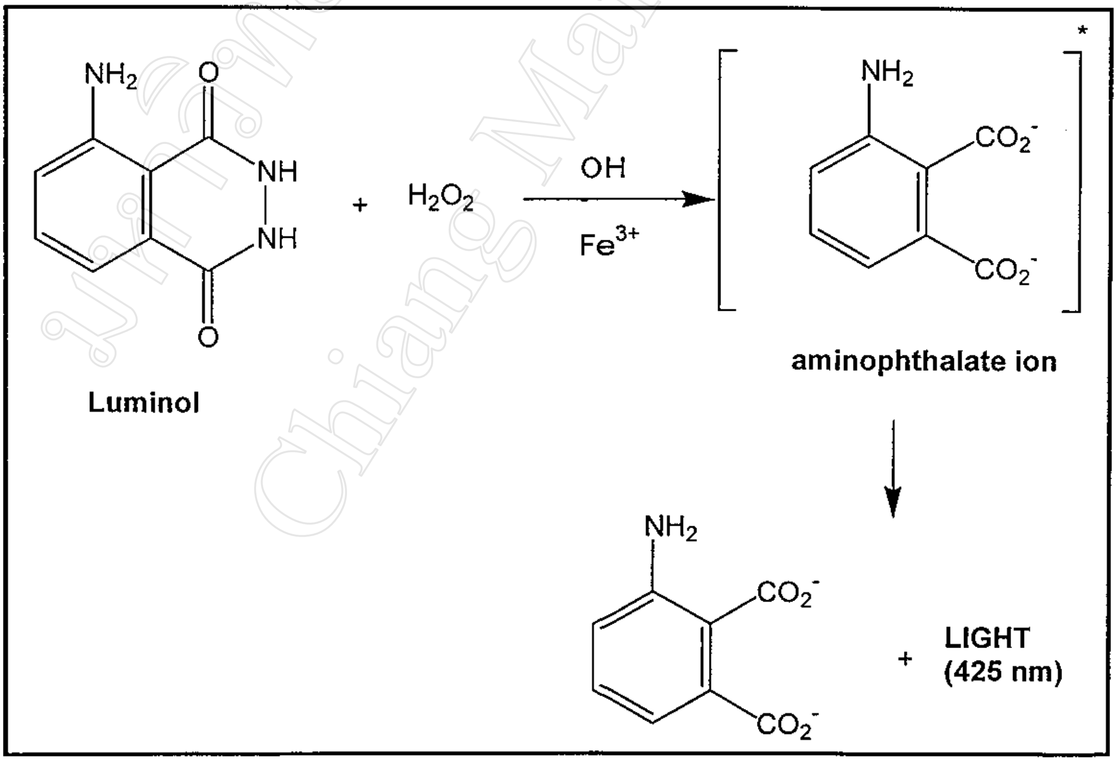

Figure 3.11 Scheme of luminol reactions producing chemiluminescence

Although determination of iron based on this reaction has been reported previously [60-66, 68-71], normal FI was employed. A common detector for chemiluminescence is a photomultiplier tube (PMT). PMTs detect the emitted photons and generated a current, which must be amplified. Liquid scintillation counters (LSCs) are usually designed with a coincident circuit, leading to a low background noise and hence a low detection limits [59]. LSCs are usually used for beta-emitting radionuclides, but applications for bioluminescence, chemiluminescence as well as alpha, positron and low energy gamma radiation are possible. A sample flow cell is positioned in between two PMTs to ensure high optical efficiency [90].

In this work attempts have been made to apply a commercial LSC, with a spiral flow cell (Packard Radiometric Flo-one®\Beta Series A-100 Model A140K) as a chemiluminescence detector and to use reverse FI-CL for determination of trace iron has been investigated.

By applying a commercial flow-through LSC which is normally for radio-HPLC, in this investigation, a very sensitive procedure using a simple set-up for determination of iron was achieved.

3.2.2 Chemiluminescence Measurements with the rFIA System

FI manifold is shown in Section 2.4.2. All investigations were performed with standard solutions using the rFIA-CL manifold (Figure 2.6).

Effect of mixing coil length

In order to ensure the efficient mixing between solutions C1 and C2 (see Figure 2.6), a mixing coil with length from 0-90 cm was used. It was found that a suitable length was 30 cm resulting in a high CL response. Shorter or longer ones cause less effective reaction or a considerable dilution, respectively.

Effect of hydrogen peroxide concentration

Hydrogen peroxide acts an oxidant for the catalytic oxidation of luminol. Therefore the higher the concentration the higher CL intensity would be expected obtain. The concentration used in most experiments was 10^{-3} M. Hydrogen peroxide can decompose quite easily resulting in bubble of O_2 in the tubing. Irreproducible CL intensity was observed if the hydrogen peroxide concentration is more than 10^{-3} M.

Effect of pH buffers

Four different buffer systems, Na_2CO_3-NaOH, Na_2BO_7-NaOH, Na_2HPO_4-NaOH and Na_3PO_4-NaOH (0.01 M), were investigated to obtain a suitable buffer for trace iron determination. The maximum chemiluminescence response was achieved in the pH range 10-11 (see Figure 3.12). Each optimal pH buffer was further investigated to obtain a suitable buffer system for rFI-CL. The carbonate buffer gave the highest sensitivity, however, it was found that signal was too high in some cases that led to the warnings indicator for light for high voltage in the LSC detector occurring when using carbonate buffer as a carrier.

The LSC detector having LED warning indicator, 'Red' and 'Green' suggesting switching 'On' and 'Off' of the instrument. If the PMTs detect extreme light, the LED indicator turns on 'Red'. Therefore the high voltage has to be switched off and reset before next re-operation.

Although it was found in this investigation that carbonate buffer gives strong CL responses, which this is similar to a findings by other [91], but concerning manipulation in resetting of the detector, it was not then considered for further use. Considering sensitivity and correlation coefficient (see Figure 3.13), the Na_2HPO_4-NaOH (pH 11) was therefore selected.

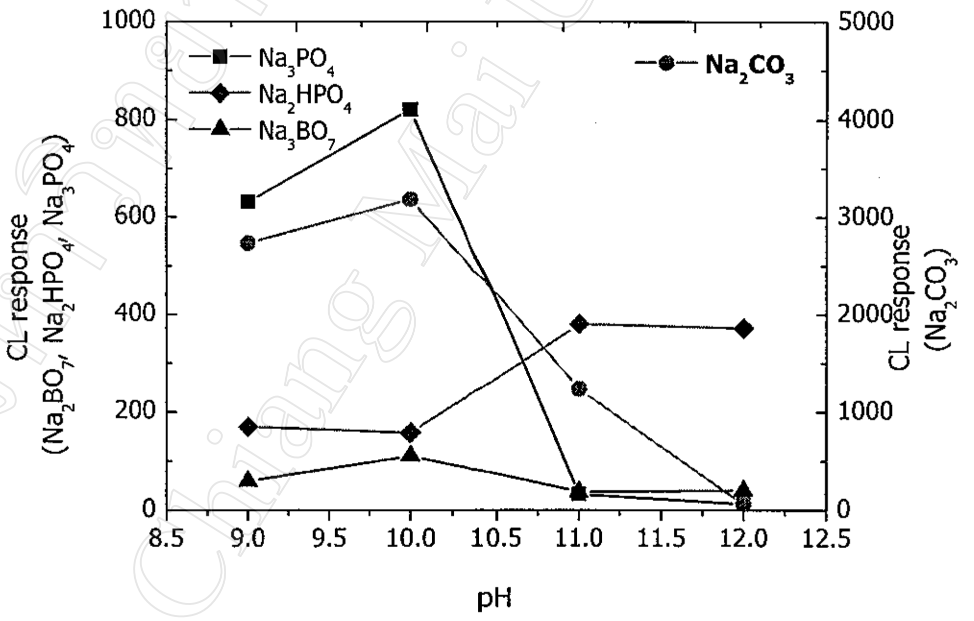

Figure 3.12 Effect of pH buffers (0.01 M) of Na_2CO_3-NaOH, Na_2BO_7-NaOH, Na_2HPO_4-NaOH and Na_3PO_4-NaOH on CL response at a luminol concentration of 2×10^{-6} M, H_2O_2 concentration of 10^{-3} M

The results of the experiments using different buffer systems given in Figure 3.12 are difficult to interpret. Little data exists on the effect of pH on the CL signal except that it is known that high pH (>10) is required. The pH could affect the CL signal in two ways. Firstly, from the reaction scheme given in Figure 3.11, increasing pH would favor oxidation of luminol to the excited aminophthalate ion molecule. Secondly, lowering the pH could promote protonation the carboxylate groups thus decreasing the concentration of the CL active form. The results of the experiments conducted here are inconclusive. Only for Na_2HPO_4 buffer did increasing, the pH increase the CL signal. In the case of the Na_3PO_4 and Na_2CO_3 buffers, increasing the pH actually inhibited the CL signal. In addition it is quite unexpected that buffers made up using the salts Na_3PO_4 and Na_2HPO_4 did not give identical results. The explanation probably lies in the complex heterogeneous nature of these 'solutions'. At high pH (>9) the Fe in the samples would precipitate as $Fe(OH)_3$. Thus we are probably dealing with a surface catalyzed CL reaction. In addition, phosphate and carbonate are likely to adsorb strongly to the iron hydroxide particle surfaces, which could well inhibit the CL reaction. A rigorous investigation of these processes is no warranted but was well beyond the scope of this thesis project.

Effect of Luminol concentration

Luminol concentrations between $2x10^{-6}$-$12x10^{-6}$ M were tested. The results are shown in Figure 3.13. The higher the amount of luminol the higher the sensitivity obtained. The concentration $8x10^{-6}$ M luminol was chosen.

Beyond this concentration, similar problems due to extreme light as stated in the previous section were observed.

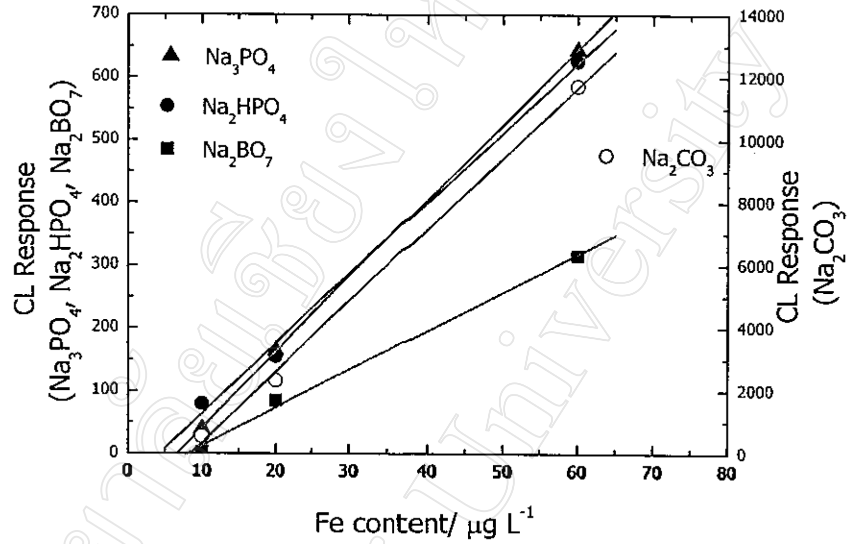

Figure 3.13 Effect of buffer medium on correlation of iron calibration graph

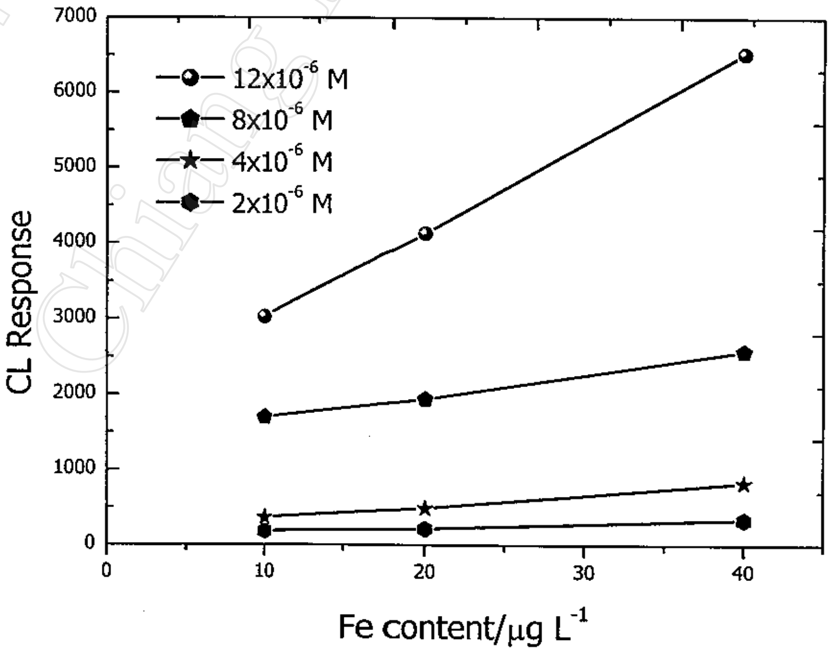

Figure 3.14 Effect of luminol concentration on CL response to added Fe (III)

Effect of carrier flow rate

Using the above established conditions the carrier flow rate was investigated. The flow rates of C1 and S (see Figure 2.6) in the manifold were considered. Since the aim was to directly combine GrFFF with rFI-CL, the flow rate of S was set equal to the carrier of GrFFF system (1.0 mL min^{-1}). The flow rate of line C1 was then varied.

The effect of flow rate on CL response was found to be not significant over the range from 1-4 mL min^{-1} as shown Figure3.15. A flow rate of 3 mL min^{-1} was observed to produce highest response. This is possible due to a compromise between mixing/reaction time and dispersion.

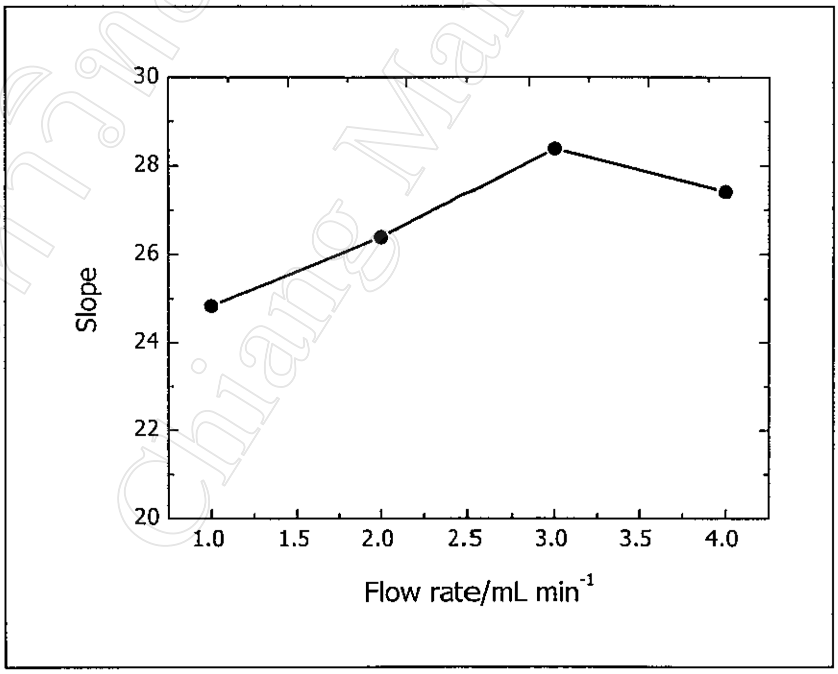

Figure3.15 Effect of the flow rate of hydrogen hydroxide reagent when merging with a series of luminol plug injections

3.2.3 Use of Laboratory-made automation for the system

In this work, a program, LabVIEW written for the software was used to record the FI signals. LabVIEW provides advantages in not only being used as a recorder but also for data evaluation and report writing [92]. It should be also be possible to control the other components of an FI-CL instrument, which could lead to a (fully) automated system.

The analog output from the CL detector was connected to a computer equipped with a LabVIEW interface and the software program was used to record the digitized data. The analog output connecting wire was donated by Mr. Subhachai Jayasvasti, Departments of Radiology, Faculty of Medicine, Chiang Mai University.

Some results using the LabVIEW interface are shown Figure 3.16.

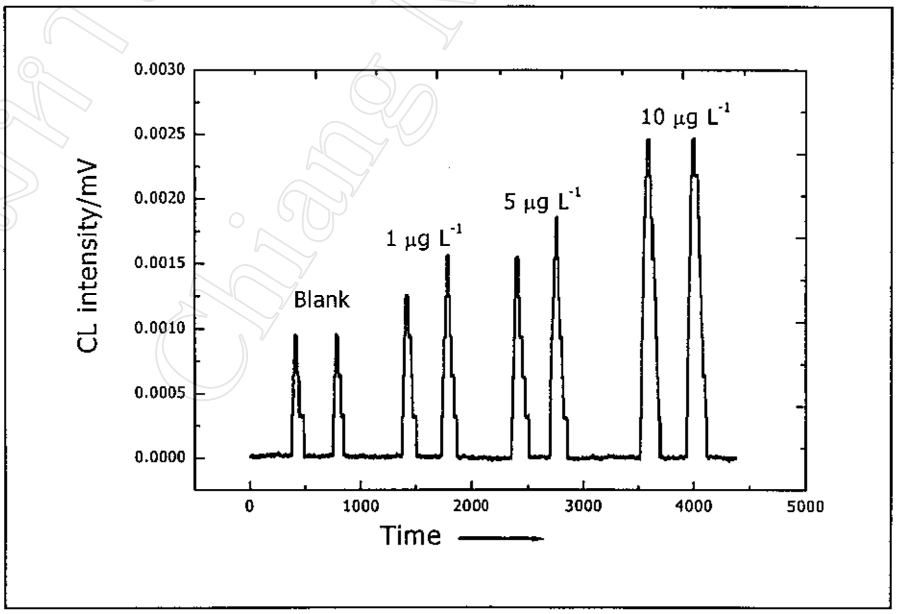

Figure 3.16 Chemiluminescence signal of the iron with the reagents used in the reaction. Iron solution concentrations were 0, 1, 5, 10 µg L^{-1} recorded by LabVIEW interfacing

Although a sensitive procedure has been achieved but as can be noticed in Figure 3.16 for a relative higher blank peak. The blank could probably be improved by using a higher grade or purified chemicals including better quality water used to make up all solutions in an experiment. Elimination of impurity/interference should be incorporated before introducing the sample into the system.

With subtraction of a blank signal, a calibration (0-10 μg L^{-1}), was found to be; y = 2276x, $r^2 = 0.9942$ with a detection limit (3σ) of 1.1 μg L^{-1} of Fe. A relative standard deviation of 3 % (n = 4) for 10 μg L^{-1} Fe was obtained [93].

The solenoid valve replacing the 6-port injection valve was employed to introduce a plug of luminol. Time-based injection was achieved by pumping the luminol plug in and controlling the flow into the rFIA with the solenoid valve as illustrated in Figure 3.17 for the operation steps. A series of injections of luminol was introduced to the rFI-CL system by pumping the luminol solution and programmed the valve status. Based on the timing of the ON-OFF steps by apply stepping voltage via a software control using LabVIEW and the luminol flow rate can then be calculated for the amount of the luminol plug in microliter. The solenoid was used in the combined of GrFFF-rFI-CL.

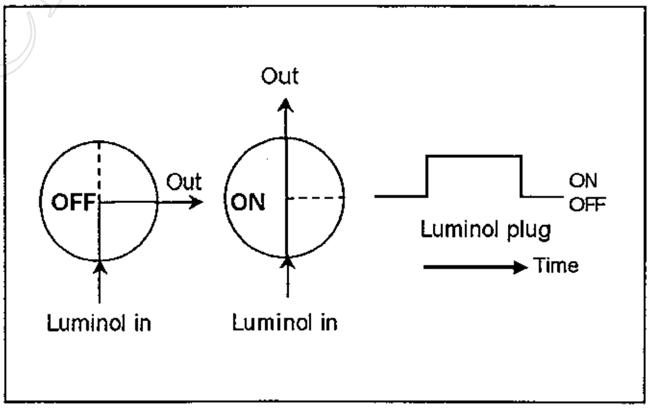

Figure 3.17 Schematic diagram of the solenoid function for injection luminol into the rFIA-CL system

3.3 Size-based iron speciation by GrFFF with rFIA or ETAAS [57]

3.3.1 Total Fe Content of the Fe Coated Silica Particles

The amount of iron on the goethite coated silica was measured by ETAAS using a conditions described in Table 2.2 after being digested with aqua regia ($HCl:HNO_3$, 3:1 v/v). The concentration of iron was found to be 12.1±0.2 mg g^{-1} and 13.7±0.7 mg g^{-1} for the 5 μm and 10 μm particles, respectively. Since the specific surface area of the 10 μm particles is larger than for the 5 μm particles, this indicates that the goethite coating is thicker on the larger particles (see discussion in Section 3.3.4 below).

Analysis of the Fe in the coated silica particles after acid digestion ($HCl:HNO_3$ 3:1 v/v) was compared with slurry sampling (suspension of particles in Milli-Q water with the same dilution). It was found that the Fe content obtained from the slurry sampling method was lower than that measured after acid digestion. The recoveries were found to be 64± 6% and 59±10% for the 5 μm and 10 μm particles, respectively.

Chen and Beckett reported almost complete recovery of Fe in a colloid sized (<1 μm) soil sample analyzed by sedimentation FFF-ETAAS [51]. This suggests that the release of Fe coatings from these larger 5 and 10 micron sized particles is less efficient or that the Fe is alternatively in a more refractory form for synthetic goethite coatings that on the natural soil colloids. However, one cannot exclude the possibility of matrix effects, caused by other elements in the particles, could lead to a reduced AAS signal.

3.3.2 Separation of the Fe Coated Silica Particles by GrFFF

Figure 3.18 shows the GrFFF fractogram of a mixture of the 5 μm and 10 μm silica particles. The first peak is the void, which contains unretained particles. The 10 μm silica eluted before the 5 μm particles as separation occurred by the steric/hyperlayer elution mechanism. Optical microscope pictures of the fractions collected at the maximum of the eluting peaks (see Figure 3.18) confirm the good separation obtained.

The diameter scale was obtained using the empirical calibration expression:

$$\log t_r = -S_d \log d \tag{3.1}$$

and measuring the elution time (t_r) at the peak maximum of the 5 μm and 10μm particles. In this equation d is the diameter of the particles and S_d is the size-based selectivity [94]. Using this data yields $S_d = 1.18$.

It was found by optical micrographs that there was a high proportion of small particles (< 1 μm) present in the 10 μm sample. These submicron particles would not be relaxed under the run conditions performed here and would thus be eluted in the unretained void peak. This was confirmed by optical micrographs of the void peak fraction (not shown in Figure 3.18).

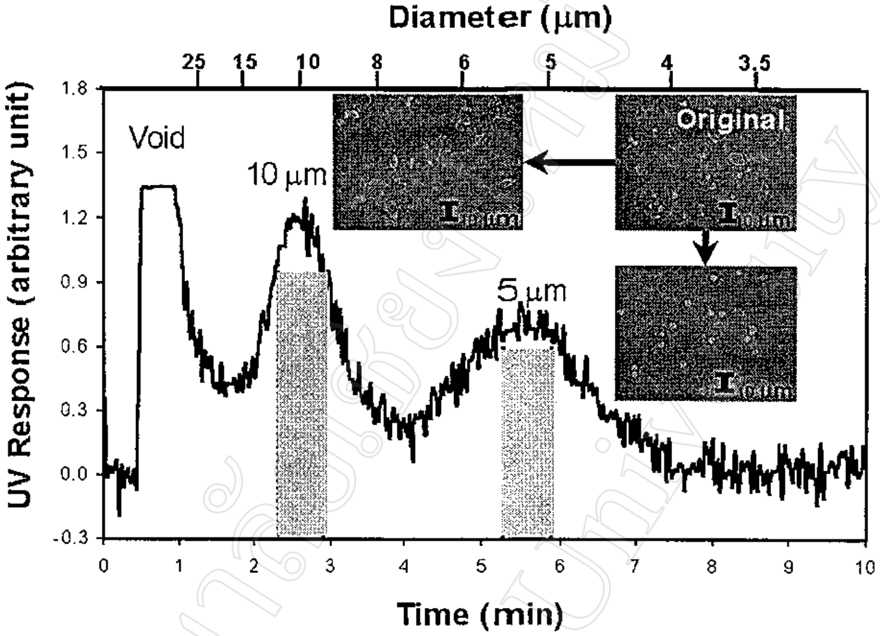

Figure 3.18 The fractogram of a mixture of 5 μm and 10 μm goethite coated silica particles and the optical microscope pictures of the original mixture and fractions collected from the shaded regions at the two peak maxima

3.3.3 GrFFF-ETAAS of the Fe Coated Silica Particles

Figure 3.19 shows the fractograms of individual GrFFF runs of the 5 μm (Figure 3.19a) and 10 μm (Figure 3.19b) Fe coated silica samples. The bar graphs represent the iron content in the collected fractions, which were determined off-line by ETAAS with slurry injection (and taking into account for 60% efficiency). It can be seen that the Fe concentration of each fraction follows quite closely the UV fractograms.

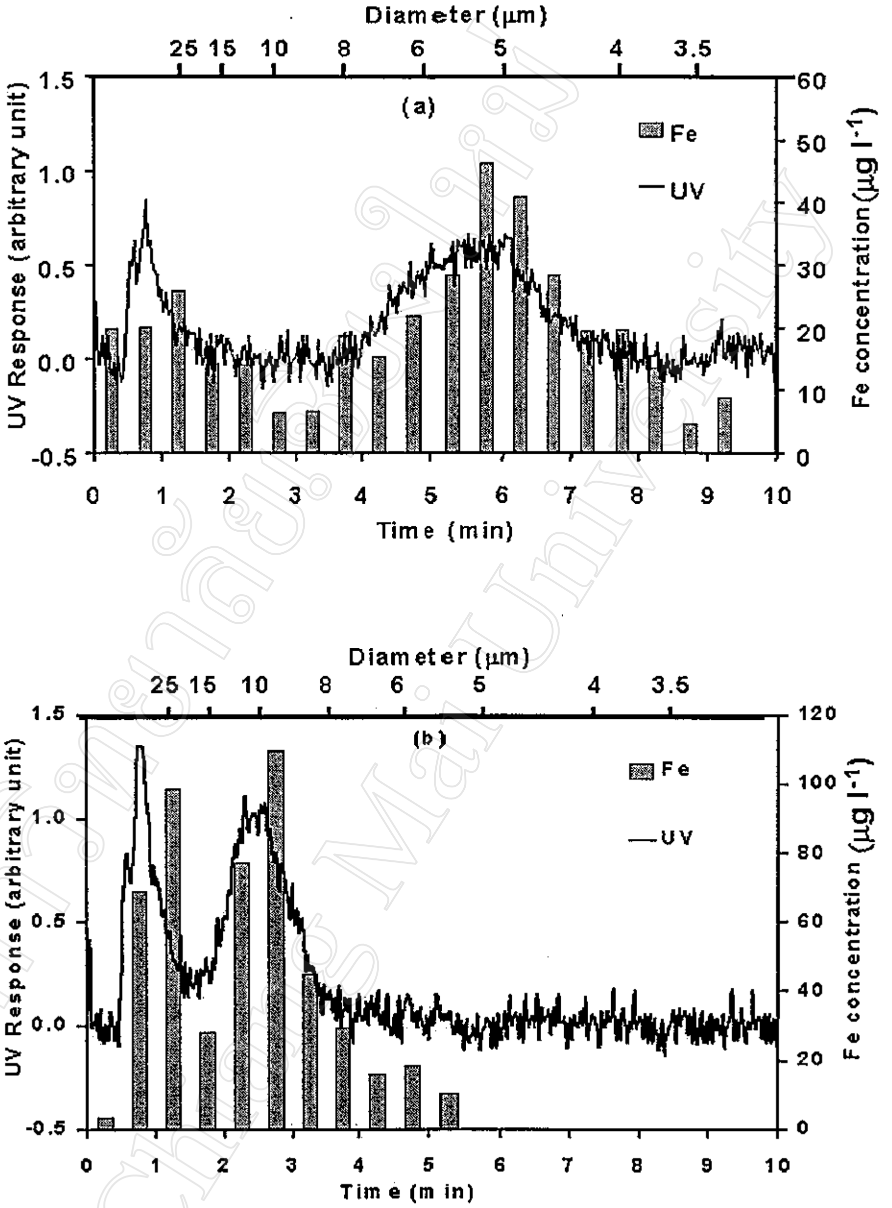

Figure 3.19 UV detector fractograms and iron contents of the fractions collected from GrFFF and determination by off-line ETAAS for the goethite coated silica, (a) 5 μm, (b) 10 μm

Computing the area under the Fe based fractograms ([Fe] vs elution time) including the void peak and comparing this with the Fe content of the whole sample digested with aqua regia, showed that 71% and 88% of the Fe on the particles was detected by slurry ETAAS, for the 5 μm and 10 μm samples, respectively. As noted above, the recovery efficiency for these larger particles seems to be less than that found by Chen and Beckett for submicron particles, (as being close to 100%) [51]. For the 10 μm particles a significant proportion of the Fe is associated with the fine particles found in the void peak which may be responsible for the higher proportion recorded by slurry ETAAS (88%) than for the spherical 5 μm particles.

3.3.4 Average Thickness of the FeOOH Layer on the Silica Particles

The thickness of the FeOOH coating of on the particles can be estimated assuming that the particle shape is spherical and the coating layer is uniform. The calculation of the thickness of goethite coated on the spherical 5 μm is illustrated below. The number of particles can be calculated from the expression:

$$n_{SiO_2} = \frac{m_{SiO_2}}{\rho_{SiO_2} \pi \frac{d^3}{6}} \qquad (3.2).$$

Where n_{SiO_2} is the number of particles injected, m_{SiO_2} is the known amount of sample mass injected, d is the diameter of the particles (5 μm), ρ_{SiO_2} is the density of the silica (2.3 mg L^{-1}) [12]. The total area of the injected particles (A_{SiO_2}) can be calculated from the equation

$$A_{SiO_2} = \pi d^2 n_{SiO_2} = \frac{6m_{SiO_2}}{\rho_{SiO_2} d} \qquad (3.3).$$

Assuming that the iron coating on the particles is goethite (FeOOH) which has a density, ρ_{FeOOH}, of 3.8 g L^{-1} [72], the total volume of the goethite coating on all of the particles injected ($V_{coating}$) is given by

$$V_{coating} = \frac{m_{FeOOH}}{\rho_{FeOOH}}, \qquad (3.4)$$

where m_{FeOOH} is the mass of the goethite in the coating. The mean thickness of the FeOOH coating on the particles (t) can be estimated assuming the particle shape is spherical. It is given by

$$t = \frac{V_{coating}}{A_{SiO_2}} = \frac{\rho_{SiO_2} m_{FeOOH}\, d}{6\,\rho_{FeOOH} m_{SiO_2}} \qquad (3.5).$$

The value of m_{FeOOH} was obtained from the Fe based fractogram using the Fe content found in the peak eluted between 3.75–7.75 min (Figure 3.19).

The calculated thickness of the goethite coating on the spherical 5 μm silica particles is found to be 5.1 nm, which is quite thin compared to the diameter of the silica particles of 5000 nm. Since neither the particle diameter nor mass increases significantly due to the goethite coating, the GrFFF retention for the coated and uncoated silica samples should be the same. The Fe content in the 10 μm sample peak was very similar, suggesting for possibility that the FeOOH coating thickness on the 10 μm particles could be approximately twice that of the 5 μm. However, the 10 μm particles are not spherical which could increase the specific surface area to some extent thus decreasing the actual coating thickness.

Since the calculated coating thickness of the goethite layer was found to be 5 nm and assuming that the coating layer was uniform, the number of Fe-O layers may be estimated to be about 12 (this was simply obtained from the sum of the covalent diameters of Fe and O). Thus if the CL reaction involves only surface Fe atoms. The maximum efficiency would be only 8%. By the rFIA-CL method, Fe contents was found to be only 5% of that obtained by ETAAS for the 5 μm particles. This could indicate that the rFIA-CL method for iron involves a surface catalyzed reaction but only a small portion (<20%) is considerable. This could be due to adsorption of the buffer ions PO_4^{3-} and CO_3^{-2} blocking surface sites.

3.3.5 GrFFF-FIA-CL of the Mixture of 5 and 10 μm of Fe Coated Silica Particles

Figure 3.20 shows the GrFFF fractogram for the mixture of 5 μm and 10 μm Fe coated silica as well as the results of the on-line Fe analysis by r-FIA-CL. The eluent from the GrFFF was continuously flowed into the r-FIA-CL for Fe analysis. Each data point of the iron content corresponds to the signal obtained from an injection of the mixture of luminol and H_2O_2 into a flowing steam of the GrFFF eluent before entering into the CL detector.

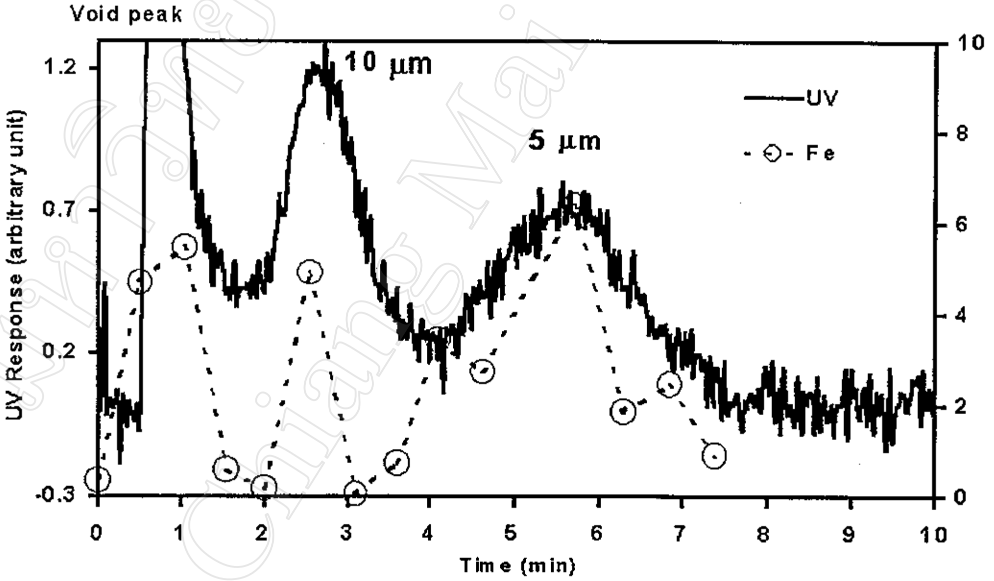

Figure 3.20 UV (solid line) and Fe concentration (open circles with dashed line) fractogram of the mixture of 10 μm and 5 μm particles. The Fe concentration was determined on-line from the GrFFF combined with FIA-CL detection.

The area under the Fe profile ([Fe] vs elution time) was used to calculate the iron content of each individual peak. The estimated Fe contents in the 5 μm and 10 μm particles were found to be 0.57 mg g^{-1} and 0.14 mg g^{-1}, respectively. These concentrations will have considerable error particularly for the 10 μm peak, which is based on only a single Fe data point. However, The iron content present in the 5 μm particles is much higher than that in the 10 μm particles, which probably suggests that the Fe content is related to the particle surface area. This is different from the trends in the Fe content obtained by GrFFF-ETAAS and after aqua regia digestion of the whole sample, where the Fe content in the two samples is approximately the same.

It is also apparent that the r-FIA-CL method detects only a small proportion of the total Fe in the sample particles. In the case of the 10 μm particles, this is only about 1% of the total Fe obtained after aqua regia digestion. About 5% of the total Fe in the 5 μm sample is detected by the CL method. FI method may only detect only 'easily released' iron on the particles. The efficiency of the luminol method is low since the Fe not extracted into solution as in the aqua regia method. It is likely that the luminol reacts only with surface Fe coatings.

3.4 Gravitational Field-Flow Fractionation with Electrothermal Atomic Absorption Spectrometry for Size-based Speciation of Iron in Clay Mineral Particles

3.4.1 Off-line and On-line Determination Iron by GrFFF with ETAAS

Off-line and on-line determination of iron by GrFFF with ETAAS can be carried out by employing the instrument set ups shown in Figure 2.8. Off-line GrFFF with ETAAS analysis was done by collecting the fractions of the eluent after passing through the GrFFF device for separation. For on-line GrFFF-ETAAS analysis, the flow from FFF unit was continuously fed into a special flow through sampler vial (Section 2.4.4). Analysis of the iron content in each fraction was obtained by slurry introduction into an electrothermal atomic absorption spectrometer (ETAAS) using the fast heating program described in Table 2.3 [95-96].

The fractogram results obtained with off-line operation for iron speciation are illustrated in Figure 3.21. It was found that the profiles obtained by off-line and on-line operations for both UV and Fe based fractograms agreed well with each other.

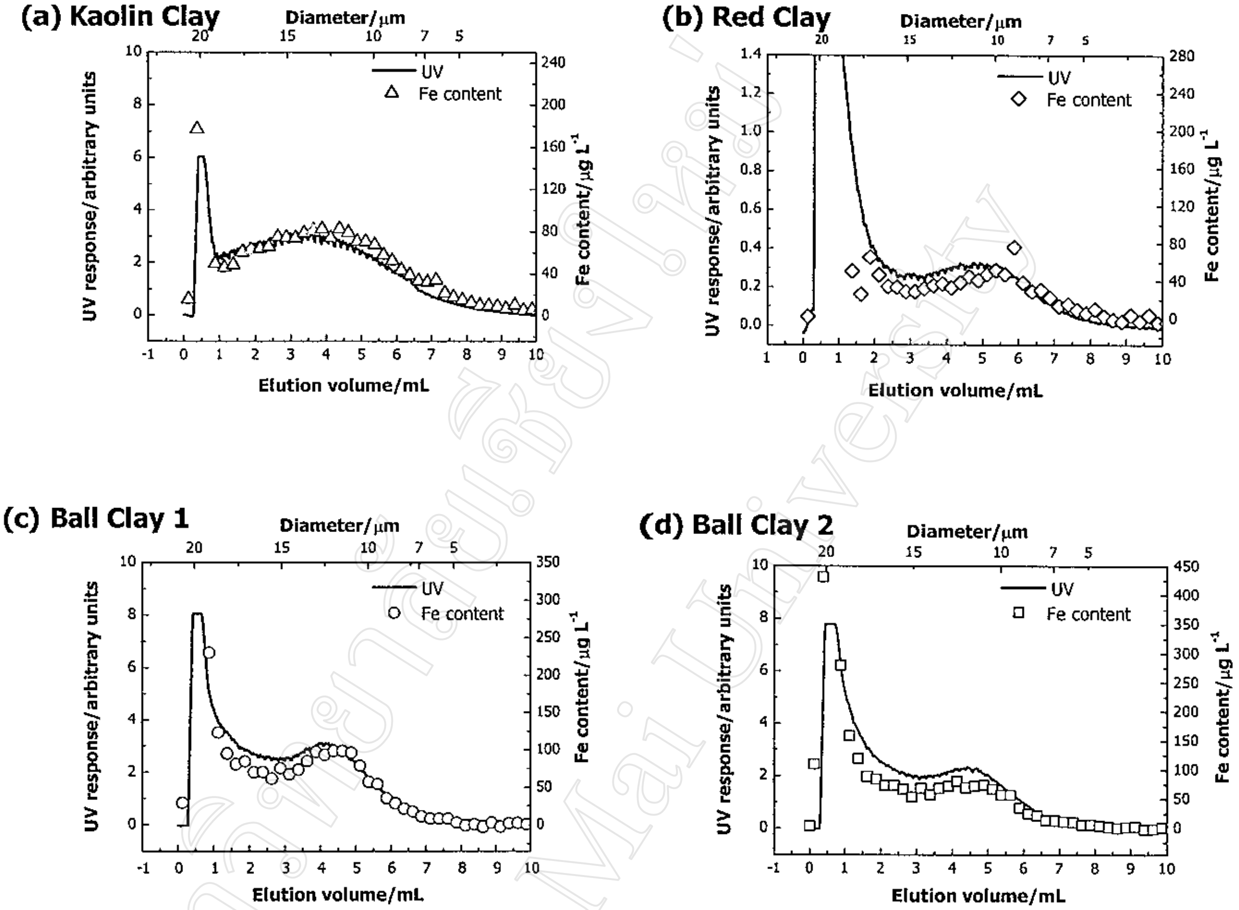

Figure 3.21 UV and Fe off-line GrFFF-ETAAS based fractograms of clay samples, (a) kaolin clay, (b) Red clay, (c) Ball clay 1 and (d) Ball clay 2

3.4.2 Development of On-line GrFFF For Iron Size-based Speciation with ETAAS

The eluent from the GrFFF separation was connected to a sampler vial in the autosampler of the ETAAS as described in the Section 2.4.4. Sample suspensions (~2 mg mL^{-1}) were injected into the GrFFF and the eluted particle.

suspension was introduced to the sampler vial continuously then overflowed to waste. The autosampler arm was set always to sample from this same position so that it introduced discrete samples of the eluent into the ETAAS. A picture of the on-line GrFFF-ETAAS instrumentation is shown in Figure 3.22.

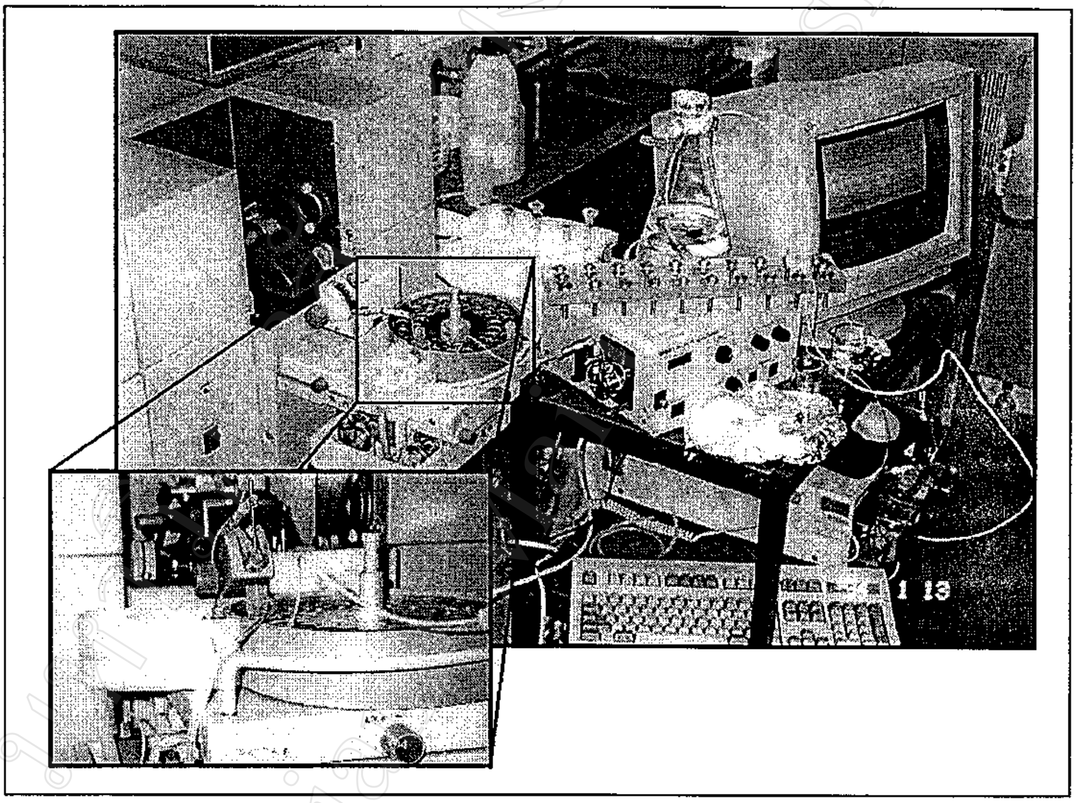

Figure 3.22 On-line GrFFF-ETAAS instrumentation.

3.4.3 Conversion From Elution Time to Diameter

By assuming that silica particles have the same density as clay particles, the conversion of the diameter scale was made employing the empirical formula [94]:

$$\log t_r = -S_d \log d_i + \log t_{r1}, \qquad (3.6)$$

where t_r is measured retention time, d is the diameter of the particles, S_d is the size selectivity and t_{r1} is a constant equal to the extrapolated value of t_r corresponding to particles of unit diameter.

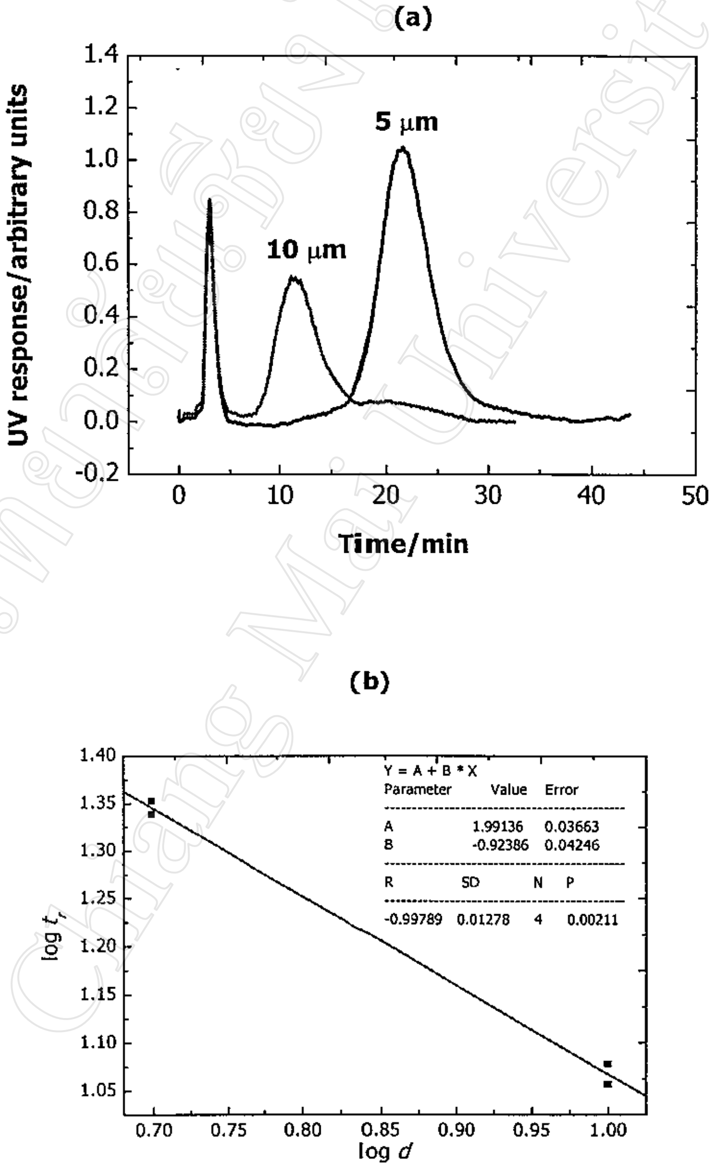

```
Y = A + B * X
Parameter      Value     Error
------------------------------------------
A              1.99136   0.03663
B              -0.92386  0.04246
------------------------------------------
R          SD          N    P
------------------------------------------
-0.99789   0.01278     4    0.00211
```

Figure 3.23 (a) Fractograms of 5 and 10 μm silica particles and (b) plot of log t_r versus log d

Figure 3.23 shows fractograms of the 5 and 10 μm silica particles and the plot of log t_r versus log d. These plots were used to generate the equation for converting the x-axis to a diameter scale as described above. In this case, the calculated selectivity using the data for the 5 μm and 10 μm silica was found to be 0.92 and t_{r1} was 98.03.

It should be noted that there may be a systematic error in this calibration due to the fact that the 5 μm silica standard particles are spherical but the 10 μm silica standard and the silica gel particles are platey in shape. It is know that platey particles experience higher lift forces than spheres of the same volume (Beckett et al) [97].

3.4.4 Conversion from UV Detector Signal to Eluted Mass

For micron size particles, the UV detector response UV_i, at point i along the FFF elution profile, is related to the mass concentration of particles of the sample in the eluent ($dm_p{}^c{}_i / dV_i$) [98-99]:

$$\frac{dm_p{}^c{}_i}{dV_i} = UV_i \cdot d_i \tag{3.7}$$

where $m_p{}^c{}_i$ is the mass of sample eluted up to elution volume V_i and d_i is the particle diameter eluting at V_i. It should be noted that the superscript c in these quantities signifies, that it is the cumulative amount eluted up to point i on the fractogram. Thus the appropriate y-axis for a particle size distribution ($dm_p{}^c{}_i / dd_i$) is given by [2]:

$$\frac{dm_{p}{}^{c}{}_{i}}{dd_i} \approx UV_i \cdot d_i \frac{\delta V_i}{\delta d_i} \tag{3.8}$$

where δd_i is the increment in d_i corresponding to increment δV_i in V at point i along the fractogram.

3.4.5 Sized-based Fe Distributions

When the GrFFF eluent was connected to the ETAAS system, the Fe content can be evaluated. The mass concentration of the Fe present in the eluent ($dm^{c}{}_{Fe_i} / dV_i$) is used to plot the Fe fractogram. This is then converted to an Fe based particle size distribution using equation:

$$\frac{dm^{c}{}_{Fe_i}}{dd_i} \approx \frac{dm^{c}{}_{Fe_i}}{dV_i} \cdot \frac{\delta V_i}{\delta d_i} \tag{3.9}$$

where $m^{c}{}_{Fe_i}$ represents the cumulative mass of Fe eluted up to digitized point i on the fractogram. The Fe based particle size distribution is obtained by plotting $dm^{c}{}_{Fe_i} / dd_i$ against particle diameter d.

3.4.6 Fe Content Distributions

The Fe concentration in the particles is given by:

$$\frac{dm^c_{Fe_i}}{dm^c_{p_i}} = \frac{dm^c_{Fe_i} / dV_i}{dm^c_{p_i} / dV_i} \propto \frac{dm^c_{Fe_i}}{dV_i} \cdot \frac{1}{UV_i d_i} \qquad (3.10).$$

The Fe concentration distribution is obtained by plotting $\frac{dm^c_{Fe_i} / dV_i}{UV_i \cdot d_i}$ i.e. $\frac{[Fe_i]}{UV \cdot d}$ against particle diameter.

For spherical particles, the mass of Fe per unit surface area can be estimated by:

$$\frac{dm^c_{Fe_i}}{dA} = \frac{dm^c_{Fe_i}}{dm^c_{p_i}} \cdot d_i = \frac{dm^c_{Fe_i} / dV_i}{UV_i} = \frac{[Fe]}{UV} \qquad (3.11).$$

Assuming all the Fe present in the form of a surface coating, the plot of $[Fe]/UV$ as a function of d represents the Fe surface coating density distributions.

3.4.7 Fractograms of Clay Samples

All clay samples are of natural origin from within Thailand. Descriptions of clay samples used in this study are as follows:

1. Kaolin sample was from Lampang province (Amphur Ma-Tha) in northern Thailand. The sample contained fine, white particles.
2. Red clay sample was from Kanchanaburi province (Amphur Muang), in middle Thailand. The sample was dark red in color.
3. Ball clay 1 and Ball clay 2 are from different sources from Payao province (Amphur Pan), in northern Thailand.

Kaolin Clay

The results are represented in Figure 3.24.

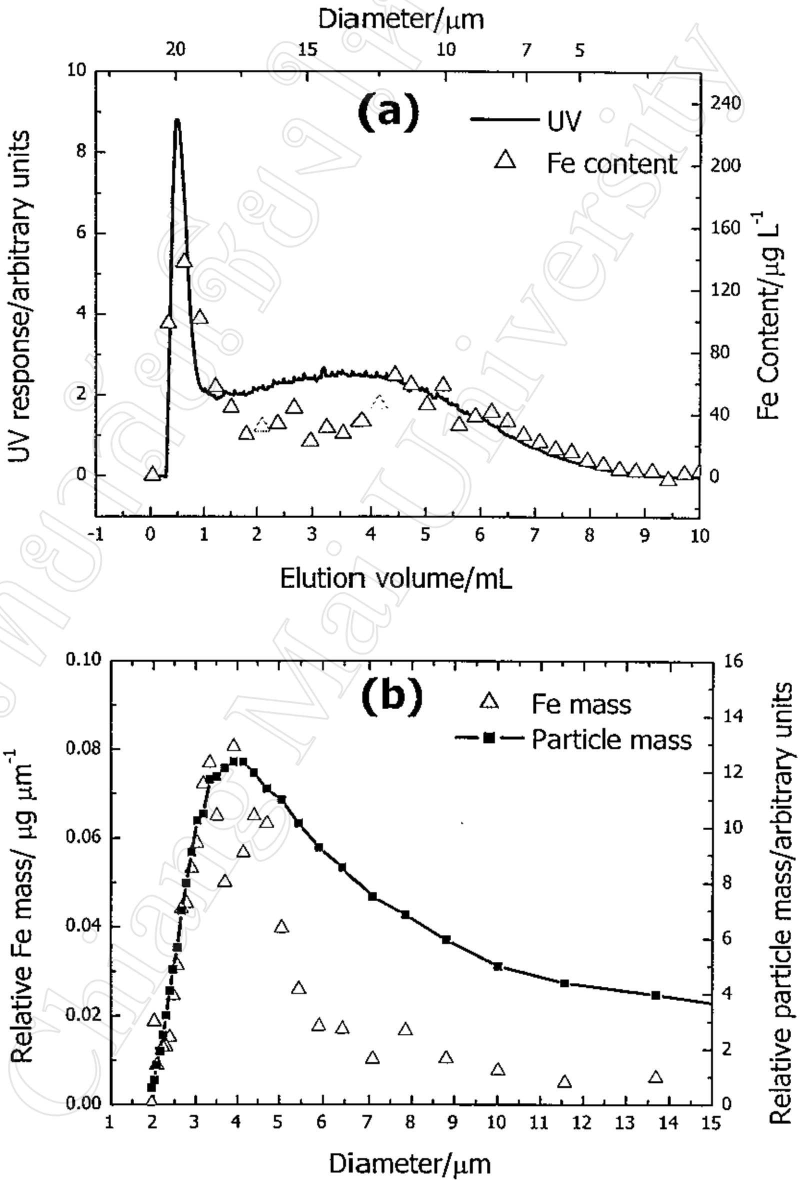

Figure 3.24 Plots for the kaolin sample (a) UV and Fe based fractograms, (b) Mass and Fe based particle size distributions, (c) Distribution of Fe concentrations in the particles as a function of diameter and (d) Mass of Fe per unit surface area distribution as a function of diameter

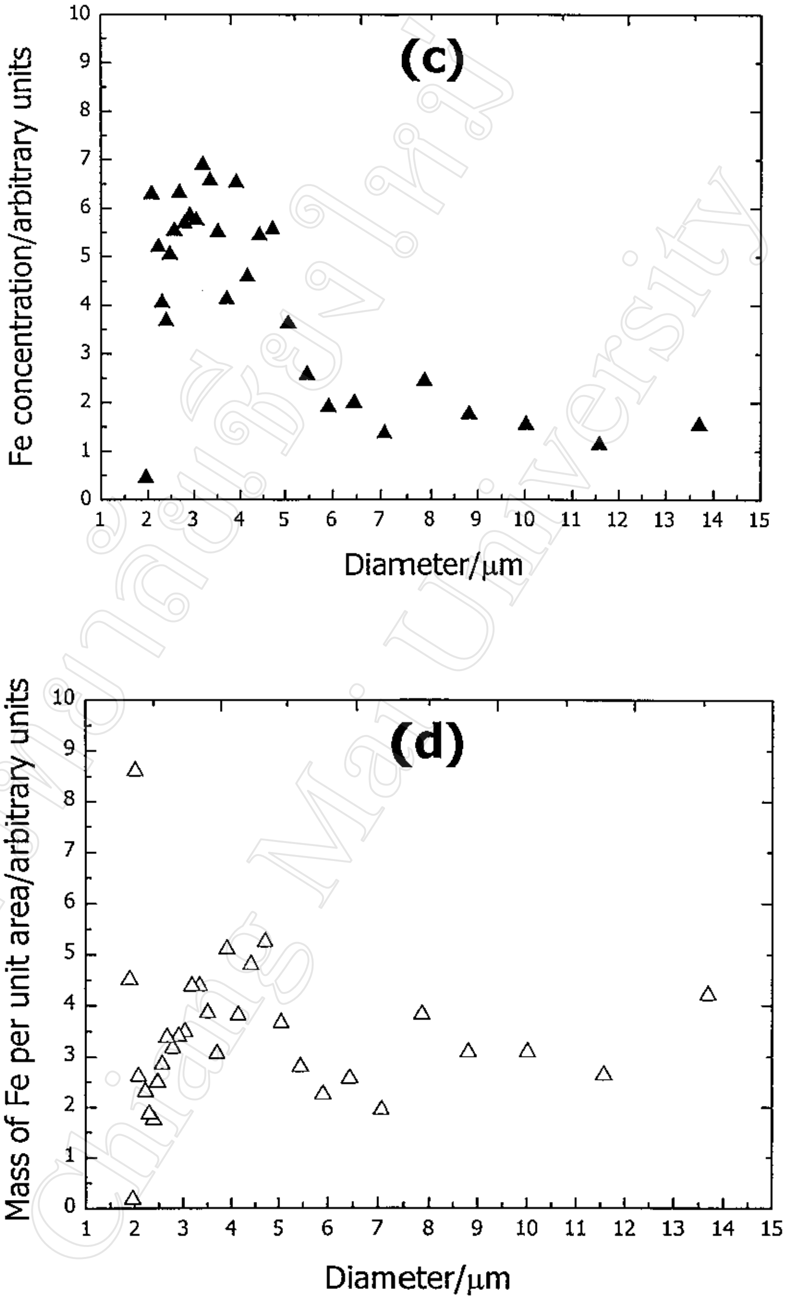

Figure 3.24 (continued) Plots for the Kaolin sample (a) UV and Fe based fractograms, (b) Mass and Fe based particle size distributions, (c) Distribution of Fe concentrations in the particles as a function of diameter and (d) Mass of Fe per unit surface area distribution as a function of diameter

Figure 3.24(a) presents the UV and Fe based fractograms of the kaolin sample. The first large sharp peak is the void peak which is not fully resolved from the sample peak. The Fe content roughly follows the UV based fractogram.

Figure 3.24(b) shows the particle mass and Fe distributions of kaolin. It was found that the kaolin sample contained particles from about 2-12 μm.

The distribution of the Fe concentration in the particles is plotted in Figure 3.24(c). The Fe content is greater in the smaller particles, which is commonly found for soil and sediment samples [22, 51]. This probably indicates that a significant proportion of the Fe is present as a surface coating on the particles.

Figure 3.24(d) shows the amount of Fe per unit surface area of particles (arbitrary units), which is the plot of [Fe]/UV. This interpretation of the plot assumes all the Fe in the particles present as coatings. A fairly constant value of Fe/area was obtained, which could indicate that Fe coating density is quite uniform. This also has been observed in several other studies [21, 22, 51, 31].

Red Clay

The results are summarized in Figure 3.25.

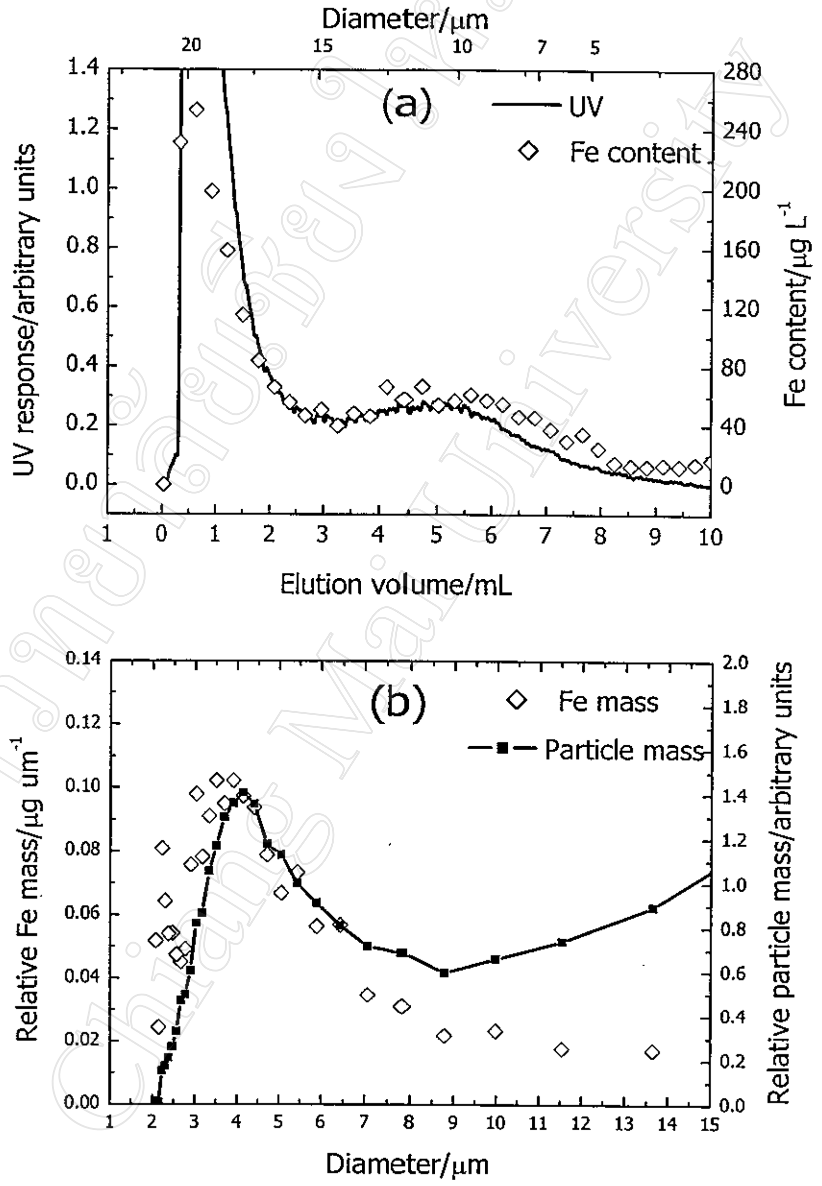

Figure 3.25 Plots for the Red clay sample (a) UV and Fe based fractograms, (b) Mass and Fe based particle size distributions, (c) Distribution of Fe concentrations in the particles as a function of diameter and (d) Mass of Fe per unit surface area distribution as a function of diameter

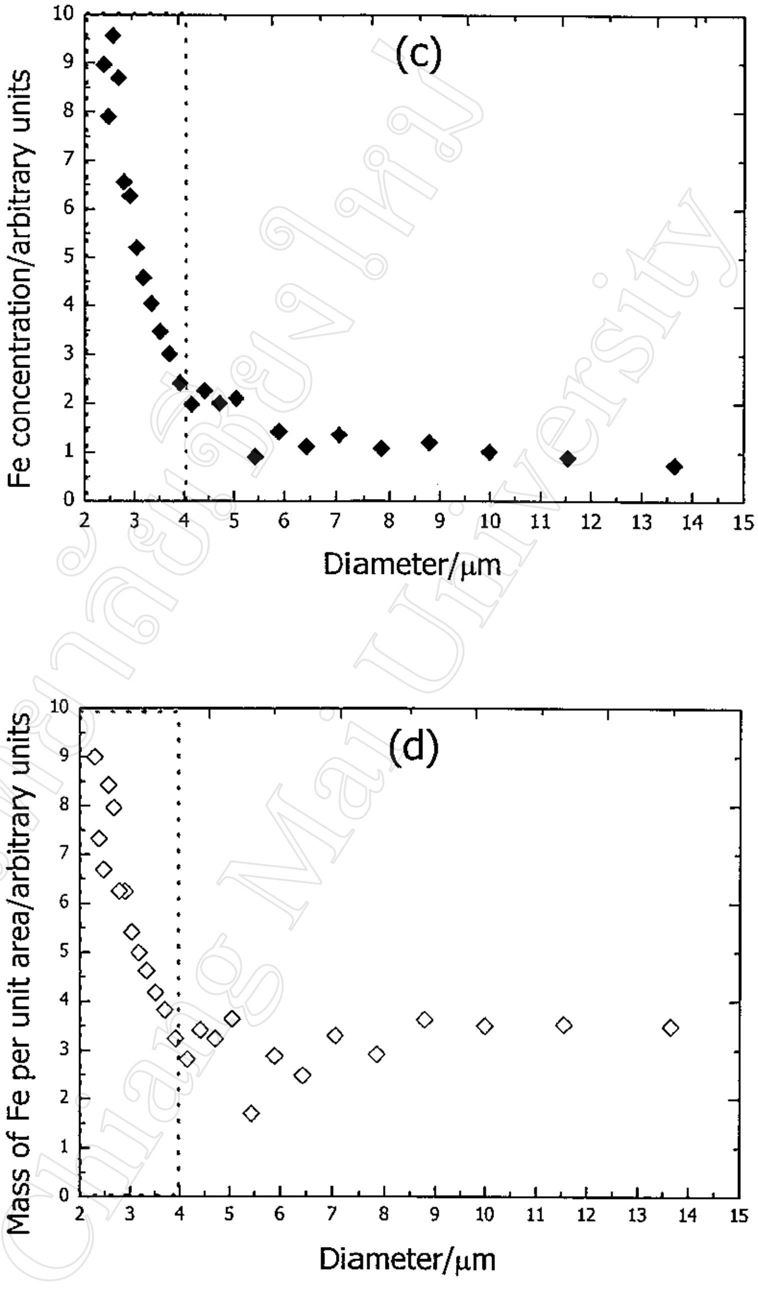

Figure 3.25 (continued) Plots for the Red clay sample (a) UV and Fe based fractograms, (b) Mass and Fe based particle size distributions, (c) Distribution of Fe concentrations in the particles as a function of diameter and (d) Mass of Fe per unit surface area distribution as a function of diameter

Figure 3.25(a) shows the UV and Fe based fractograms for the Red clay. The fractogram has a large void peak and the sample had a peak maximum at an elution volume of about 5 mL. The UV fractogram follows closely the Fe based fractogram.

The mass distributions of particles and iron are given in Figure 3.25(b) and the distribution of Fe concentrations in the particles is in Figure 3.25(c). These plots indicate the Fe content increases as size decreases. There is a particularly strong increase of Fe concentration for particles <4 μm.

Figure 3.25(d) is a plot of iron present per unit surface area. It is roughly constant for particles above 4 μm, but increases rapidly for particles <4 μm. This may indicate an increase in the Fe coating density with decreasing size. However, it may be due to an increase in the iron contained within the particles. The red color of the sample suggests the presence of Fe(III) based minerals such as goethite, hematite or magnetite.

Ball Clay 1 and Ball Clay 2

The results are presented in Figure 3.26 and Figure 3.27.

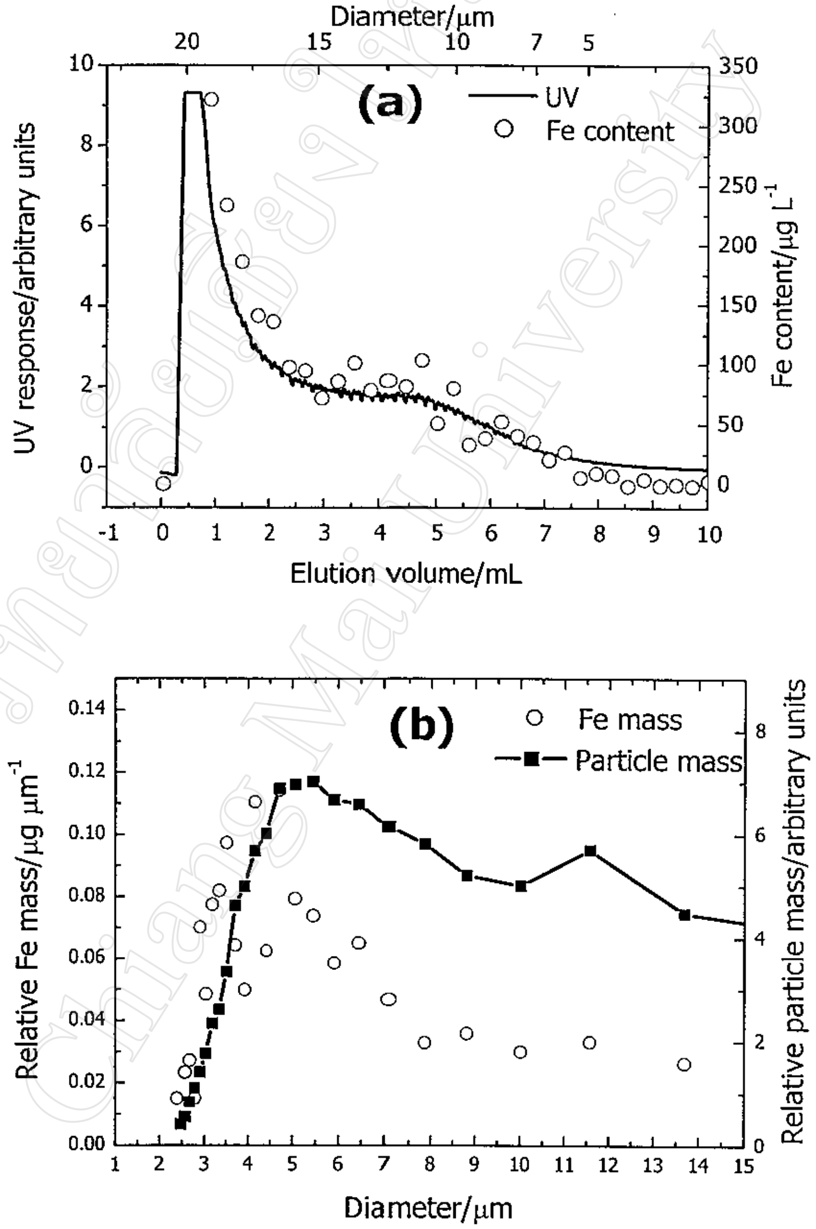

Figure 3.26 Plots for the Ball clay 1 sample (a) UV and Fe based fractograms, (b) Mass and Fe based particle size distributions, (c) Distribution of Fe concentrations in the particles as a function of diameter and (d) Mass of Fe per unit surface area distribution as a function of diameter

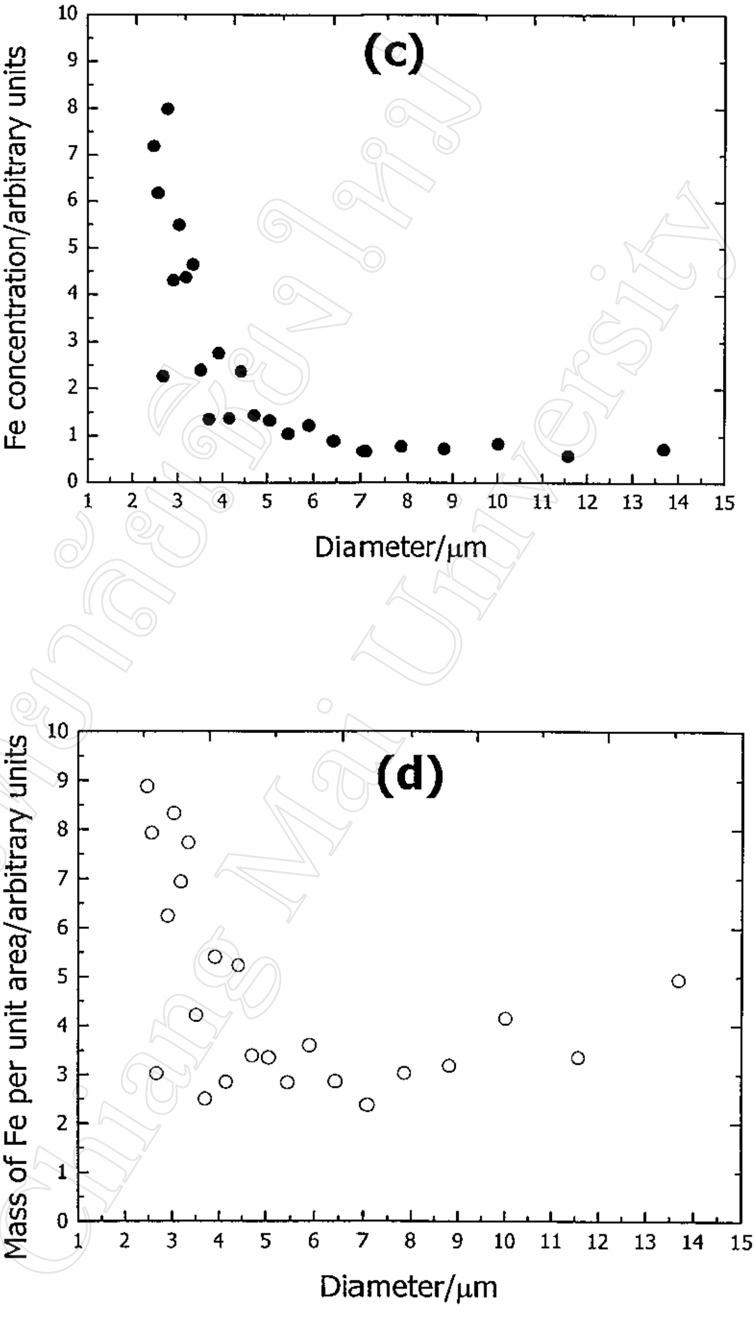

Figure 3.26 (continued) Plots for the Ball clay 1 sample (a) UV and Fe based fractograms, (b) Mass and Fe based particle size distributions, (c) Distribution of Fe concentrations in the particles as a function of diameter and (d) Mass of Fe per unit surface area distribution as a function of diameter

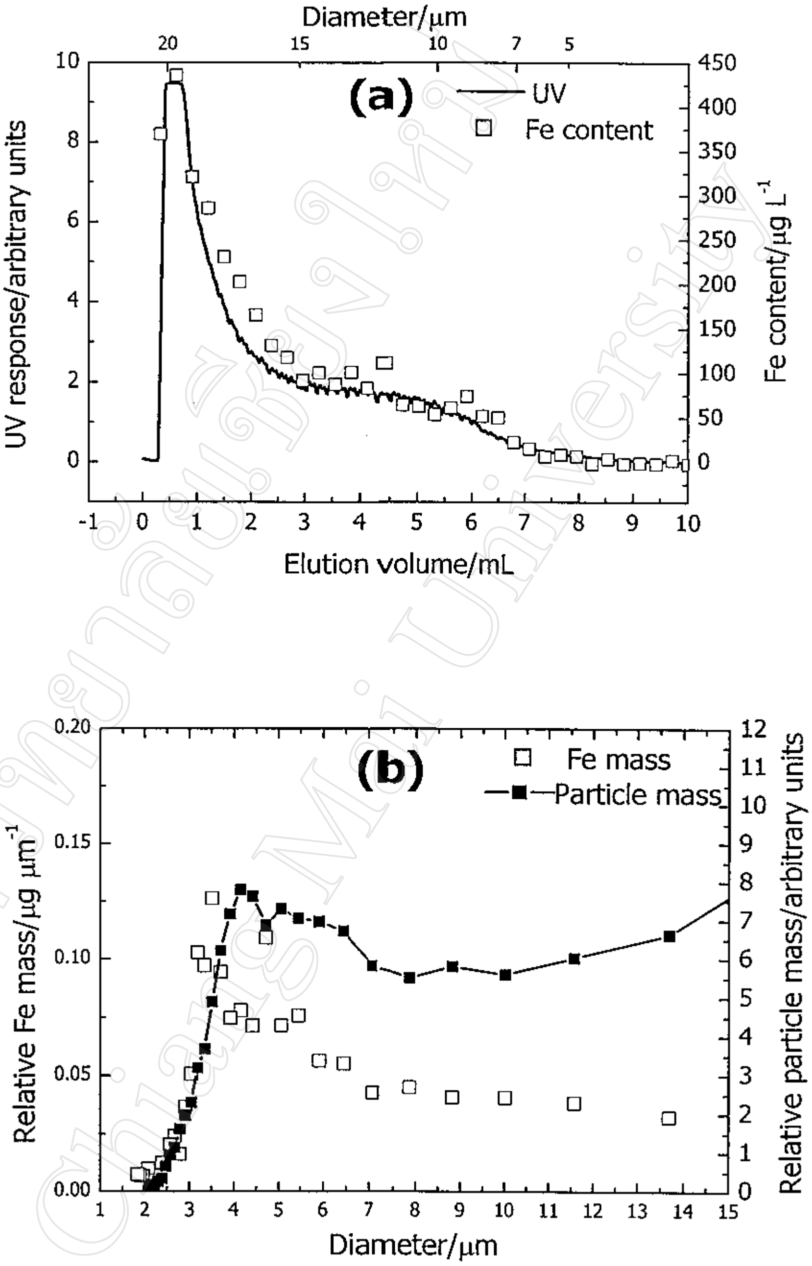

Figure 3.27 Plots for the Ball clay 2 sample (a) UV and Fe based fractograms, (b) Mass and Fe based particle size distributions, (c) Distribution of Fe concentrations in the particles as a function of diameter and (d) Mass of Fe per unit surface area distribution as a function of diameter

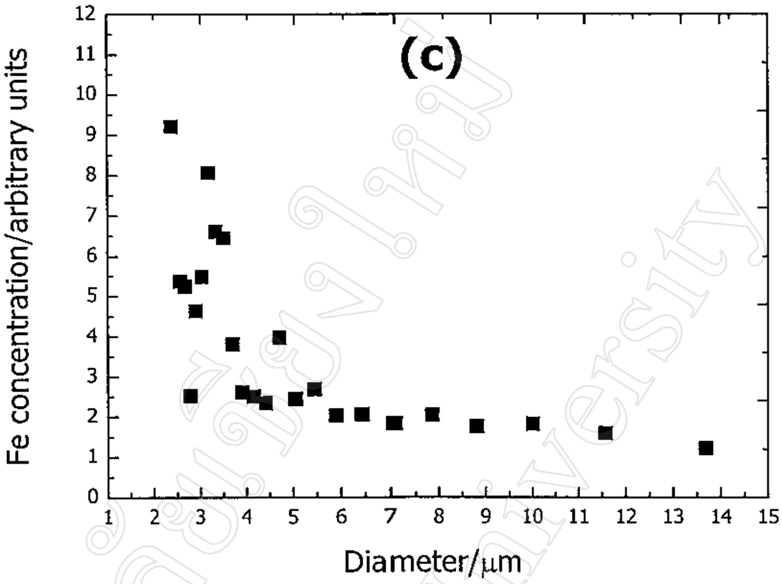

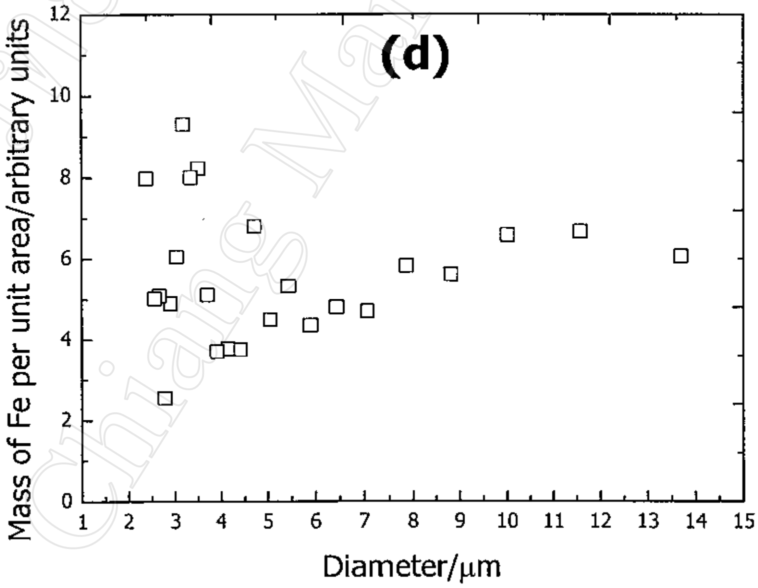

Figure 3.27 (continued) Plots for the Ball clay 2 sample (a) UV and Fe based fractograms, (b) Mass and Fe based particle size distributions, (c) Distribution of Fe concentrations in the particles as a function of diameter and (d) Mass of Fe per unit surface area distribution as a function of diameter

The trends are very similar to that of the red clay described above. The fractograms of the UV and Fe signals for ball clays 1 and 2 are shown in Figure 3.26(a) and Figure 3.27(a), respectively. The UV and Fe fractograms in both samples are similar to each other. The size distributions and Fe concentration profiles reveal a decrease in Fe content with increasing particle size. The mass of Fe per unit area distribution for both ball clays indicate that there is a constant Fe coating above about 5 μm. For Ball clay 1, the Fe concentration per unit surface area increases dramatically as the size decreases below 5 μm. This could be due to either an increase in the Fe surface coating density or a change to more Fe rich minerals in the smaller particles. For Ball clay 2 the observed data for particles below 5 μm are too scattered to make any conclusions.

3.4.8 Efficiency of Fe Analysis by GrFFF-ETAAS

An evaluation was carried out on the effectiveness of the slurry ETAAS method for Fe analysis after GrFFF separation. Summation of the iron amounts in each fraction across the entire Fe based fractogram (including the void peak) provides an estimate amount of Fe containing in the samples. This was done by integration of the area under the Fe based fractograms obtained by both off-line and on-line operation. The results were compared with the total iron content of the original sample analyzed by flame atomic absorption spectrometry after being digested with aqua regia. This comparison is presented in Figure 3.28.

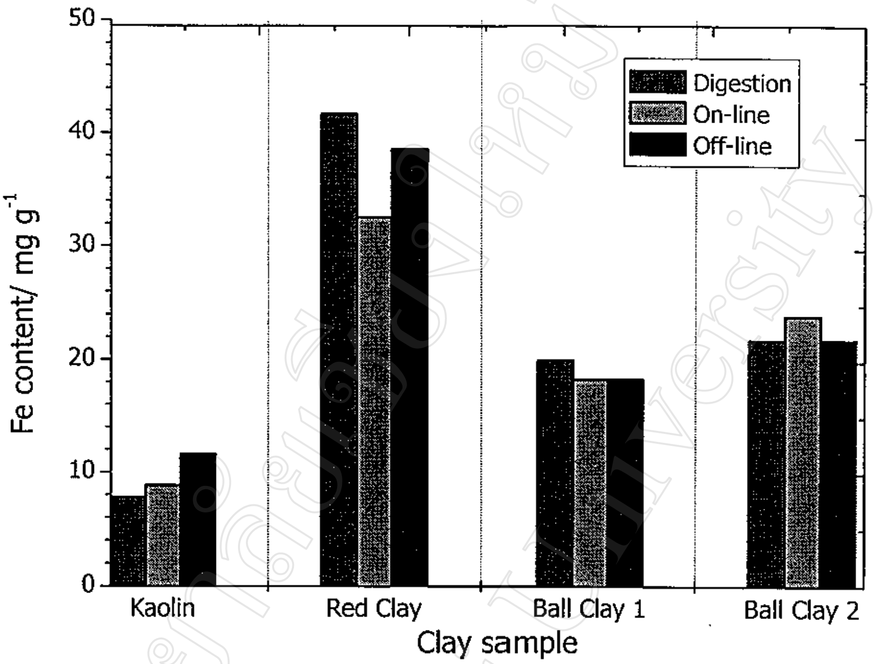

Figure 3.28 Comparison of the Fe content obtained from GrFFF-ETAAS (both off-line and on-line slurry injection) and the total Fe content of the digested original sample

It can be seen that the efficiencies of the GrFFF-ETAAS method (both off-line and on-line slurry injection) agreed reasonably well with the digestion analysis.

Using the mean value of all three methods, the percentage deviations from the mean of each method can be calculated as shown in Table 3.1. It was found that the deviation from mean for the digestion, on-line and off-line were 3-18%, 3-16% and 3-23%, respectively.

Assuming that the digestion method gave the most accurate, estimate of the total Fe content of the sample, the percentage deviations from this value for the slurry methods were found to be 8-22 % for the on-line method and 0-50% for off-line method.

Table 3.1 Percentage deviation from either the mean value or Fe content of total digested sample calculated for the four clay samples

Sample	%Deviation of Fe content from the mean value [(a)]			%Deviation of Fe content from the digested value [(b)]	
	Digested	On-line	Off-line	On-line	Off-line
Kaolin clay	18	6	23	14	50
Red clay	11	13	3	22	7
Ball clay1	6	3	3	8	8
Ball clay 2	3	6	3	10	0

(a) % Deviation of Fe content the mean value= $\frac{(Method_i - Mean)\text{x}100}{Mean}$

(b) % Deviation of Fe content from digested value= $\frac{(Method_i - Digest)\text{x}100}{Digest}$

The mean value was for the three methods
(method$i$; i was the digested, on-line and off-line method)

It was found that for the kaolin and Ball clay 2 samples, the slurry results were higher than those obtained from the digestion analysis. This suggested that there could be other errors in the analysis in addition to inefficient slurry atomization. Thus it is reasonable to conclude from the results in Table 3.1 that the slurry efficiency is quite good. However, optimization of the slurry method is required to improve the overall accuracy of the Fe analysis.